A global observational analysis to understand changes in air quality during exceptionally low anthropogenic emission conditions

Ranjeet S. Sokhi[1*], Vikas Singh[2], Xavier Querol[3], Sandro Finardi[4], Admir Créso Targino[5], Maria de Fatima Andrade[6], Radenko Pavlovic[7], Rebecca M. Garland[8,9,10], Jordi Massagué[3,11], Shaofei Kong[12], Alexander Baklanov[13], Lu Ren[13], Oksana Tarasova[13], Greg Carmichael[14], Vincent-Henri Peuch[15], Vrinda Anand[17], Graciela Arbilla[18], Kaitlin Badali[19], Gufran Beig[17], Luis Carlos Belalcazar[20], Andrea Bolignano[21], Peter Brimblecombe[22], Patricia Camacho[16], Alejandro Casallas[23, 31], Jean-Pierre Charland[19], Jason Choi[24], Eleftherios Chourdakis[25], Isabelle Coll[26], Marty Collins[27], Josef Cyrys[28], Cleyton Martins da Silva[29], Alessandro Domenico Di Giosa[21], Anna Di Leo[30], Camilo Ferro[31], Mario Gavidia-Calderon[6], Amiya Gayen[32], Alexander Ginzburg[34], Fabrice Godefroy[35], Yuri Alexandra Gonzalez[20], Marco Guevara-Luna[36], Sk. Mafizul Haque[32], Henno Havenga[37], Dennis Herod[38], Urmas Hõrrak[39], Tareq Hussein[40], Sergio Ibarra[6], Monica Jaimes[16], Marko Kaasik[39], Ravindra Khaiwal[41], Jhoon Kim[42], Anu Kousa[43], Jaakko Kukkonen[44,1], Markku Kulmala[40], Joel Kuula[44], Nathalie La Violette[45], Guido Lanzani[30], Xi Liu[12], Stephanie MacDougall[46], Patrick M. Manseau[7], Giada Marchegiani[21], Brian McDonald[47], Swasti Vardhan Mishra[32], Luisa T. Molina[33], Dennis Mooibroek[48], Suman Mor[49], Nicolas Moussiopoulos[25], Fabio Murena[50], Jarkko V. Niemi[45], Steffen Noe[51], Thiago Nogueira[6], Michael Norman[52], Juan Luis Pérez-Camaño[53], Tuukka Petäjä[40], Stuart Piketh[37], Aditi Rathod[17], Ken Reid[54], Armando Retama[55], Olivia Rivera[16], Néstor Y. Rojas[20], Jhojan P. Rojas[56], Roberto San José[53], Odón Sánchez[57], Rodrigo J. Seguel[58], Salla Sillanpää[44], Yushan Su[59], Nigel Tapper[60], Antonio Terrazas[16], Hilkka Timonen[44], Domenico Toscano[50], George Tsegas[25], Guus J. M. Velders[48], Christos Vlachokostas[25], Erika von Schneidemesser[61], Rajasree VPM[1], Ravi Yadav[17], Rasa Zalakeviciute[62] and Miguel Zavala[33]

*Corresponding author (r.s.sokhi@herts.ac.uk)

[1] Centre for Atmospheric and Climate Physics (CACP) and Centre for Climate Change Research (C3R), University of Hertfordshire, Hatfield, Hertfordshire, UK
[2] National Atmospheric Research Laboratory, Gadanki, AP, India
[3] Institute of Environmental Assessment and Water Research (IDAEA), Spanish Research Council (CSIC), Barcelona, Spain
[4] ARIANET, Milan, Italy
[5] Graduate Program in Environment Engineering, Federal University of Technology, Londrina, Brazil
[6] Departamento de Ciências Atmosféricas, Universidade de São Paulo, São Paulo, Brazil
[7] Meteorological Service of Canada, Environment and Climate Change Canada, Dorval, Canada
[8] Council for Scientific and Industrial Research, Pretoria, South Africa
[9] Unit for Environmental Sciences and Management, North-West University, Potchefstroom, South Africa
[10] Department of Geography, Geo-informatics and Meteorology, University of Pretoria, Pretoria, South Africa
[11] Department of Mining, Industrial and ICT Engineering, Universitat Politècnica de Catalunya, BarcelonaTech (UPC), Barcelona, Spain
[12] Department of Atmospheric Sciences, School of Environmental Studies, China University of Geosciences, Wuhan 430074, China
[13] Science and Innovation Department, World Meteorological Organization (WMO), Geneva, Switzerland
[14] Center for Global and Regional Environmental Research, University of Iowa, Iowa City, United States
[15] ECMWF, European Centre for Medium-Range Weather Forecasts, Shinfield Park, Reading, UK
[16] Secretaria del Medio Ambiente de la Ciudad de México (SEDEMA), Mexico City, Mexico
[17] Indian Institute of Tropical Meteorology, Pune, Ministry of Earth Sciences, Govt. of India, India
[18] Universidade Federal do Rio de Janeiro, Rio de Janeiro, Brazil
[19] Analysis and Air Quality Section, Air Quality Research Division, Environment and Climate Change Canada, Ottawa, Canada
[20] Universidad Nacional de Colombia, Bogotá, Colombia
[21] Agenzia Regionale di Protezione dell'Ambiente del Lazio, via Boncompagni 101, 00187 Rome, Italy
[22] Department of Marine Environment and Engineering, National Sun Yat Sen University, Kaohsiung, Taiwan
[23] Earth System Physics, The Abdus Salam International Centre for Theoretical Physics (ICTP), Trieste, Italy
[24] Environment Protection Authority Victoria, Centre for Applied Sciences, Macleod, Australia

[25] Laboratory of Heat Transfer and Environmental Engineering, Aristotle University, Thessaloniki, Greece.
[26] Université Paris-Est Créteil and Université de Paris, CNRS, LISA, Creteil, France
[27] Air Monitoring Operations, Resource Stewardship Division, Environment and Parks, Edmonton, Canada
[28] Institute of Epidemiology, Helmholtz Zentrum München, Neuherberg, Germany
[29] Universidade Veiga de Almeida, Rio de Janeiro, Brazil
[30] Agenzia Regionale di Protezione dell'Ambiente della Lombardia, Milano, Italy
[31] Escuela de Ciencias Exactas e Ingenieria, Universidad Sergio Arboleda, Bogotá, Colombia
[32] Department of Geography, University of Calcutta, Kolkata, India
[33] Molina Center for Energy and the Environment, California, USA
[34] A.M. Obukhov Institute of Atmospheric Physics, Moscow, Russia
[35] Service de l'Environnement, Division du Contrôle des Rejets et Suivi Environnemental, Montréal, Canada
[36] Conservación, Bioprospección y Desarrollo Sostenible, Universidad Nacional Abierta y a Distancia, Bogotá, Colombia
[37] Unit for Environmental Sciences and Management, North-West University, Potchefstroom, South Africa
[38] National Smog Analysis, Analysis and Air Quality Section, Air Quality Research Division, Environment and Climate Change Canada, Ottawa, Canada
[39] Institute of Physics, University of Tartu, Tartu, Estonia
[40] Institute for Atmospheric and Earth System Research (INAR/Physics), University of Helsinki, Helsinki, Finland
[41] Department of Community Medicine and School of Public Health, PGIMER, Chandigarh, India
[42] Department of Atmospheric Sciences, Yonsei University, Seoul, South Korea
[43] Helsinki Region Environmental Services Authority, Helsinki, Finland
[44] Finnish Meteorological Institute, Helsinki, Finland
[45] Direction de la qualité de l'air et du climat, Direction générale du suivi de l'état de l'environnement, Ministère de l'Environnement et de la Lutte contre les changements climatiques Québec, Canada
[46] Air Quality Monitoring & Reporting, Nova Scotia Environment, Halifax, Canada
[47] National Oceanic and Atmospheric Administration, Chemical Sciences Laboratory, Boulder, USA
[48] National Institute for Public Health and the Environment (RIVM), Bilthoven, Netherlands
[49] Department of Environment Studies, Punjab University, Chandigarh, India
[50] Department of Chemical, Material and Production Engineering (DICMAPI), Naples, Italy
[51] Estonian University of Life Sciences, Tartu, Estonia
[52] Environment and Health Administration, City of Stockholm, Sweden
[53] Computer Science School, ESMG, Technical University of Madrid (UPM), Madrid, Spain
[54] Air Quality and Climate Change, Metro Vancouver Regional District, Burnaby, Canada
[55] Independent Researcher, Mexico City, Mexico
[56] National Meteorology and Hydrology Service, Lima, Peru
[57] Atmospheric Pollution Research Group, Universidad Nacional Tecnológica de Lima Sur, Lima, Peru
[58] Center for Climate and Resilience Research (CR)2, Department of Geophysics, University of Chile, Santiago, Chile
[59] Environmental Monitoring and Reporting Branch, Ontario Ministry of the Environment, Conservation and Parks, Toronto, Canada
[60] School of Earth, Atmosphere and Environment, Monash University, Clayton, Australia
[61] Institute for Advanced Sustainability Studies, Potsdam, Germany
[62] Grupo de Biodiversidad, Medio Ambiente y Salud (BIOMAS), Universidad de Las Americas, Quito, Ecuador

Supplementary Material

The supplementary material is subdivided into Sections having the same name and numbers of the manuscript Sections. This choice allows the reader to easily access Figures and Tables referred in the manuscript. Tables and Figures are identified by tree numbers indicating: section, subsection, and figure number as, e.g., Figure S3.2.12.

S2.1 Description of cities and regions

Table S2.1.1. Geographic, climatic and demographic features of the analysed cities.

Acr	City	Country	Continent	City/Metro	msl height (m)	Population (millions)	Climate (Koppen)	Winter house heating season
URU	Urumqi	China	Asia	M	800	3.6	Dwb	October-April
SHE	Shenyang	China	Asia	M	51	8.3	Dwa	November-March
XIA	Xi'an	China	Asia	M	400	10.2	Cwa	November-March
BEI	Beijing	China	Asia	M	44	21.5	Dwa	November-March
SHA	Shanghai	China	Asia	M	4	24.3	Cfa	none[1]
JIN	Jinan	China	Asia	M	148	8.9	Cwa	November-March
ZHE	Zhengzhou	China	Asia	M	108	10.4	Cwa	November-March
CHE	Chengdu	China	Asia	M	500	16.6	Cwa	none[1]
WUH	Wuhan	China	Asia	M	20	11.2	Cwa	none[1]
GUA	Guangzhou	China	Asia	M	7	15.3	Cfa	none[1]
SEO	Seoul	South Korea	Asia	C	38	9.7	Dwa	October-March
DAE	Daegu	South Korea	Asia	M	49	2.4	Cfa	October-March
AMR	Amritsar	India	Asia	M	234	1.2	BSh	November-February[2]
CHA	Chandigarh	India	Asia	M	320	1.1	Cwa/BSh	November-February[2]
DEL	Delhi	India	Asia	M	220	16.8	Cwa/BSh	November-February[2]
KOL	Kolkata	India	Asia	M	10	14.1	Aw	December-January[2]
PUN	Pune	India	Asia	M	560	5.1	Aw/BSh	November-February[2]
HYD	Hyderabad	India	Asia	M	540	7.7	BSh	December-January[2]
CHN	Chennai	India	Asia	M	6	8.7	Aw	December-January[2]
BEH	Bengaluru	India	Asia	M	920	8.5	Aw	December-January[2]
HEL	Helsinki	Finland	Europe	M	26	1.2	Dfb	October-April
STO	Stockholm	Sweden	Europe	C	15	1.0	Dfb	October-April
TAL	Tallinn	Estonia	Europe	C	30	0.4	Dfb	September-May
TAR	Tartu	Estonia	Europe	C	50	0.1	Dfb	September-May
MOS	Moscow	Russia	Europe	M	150	12.7	Dfb	October-April
LON	London	UK	Europe	M	14	8.9	Cfb	October-April
AMS	Amsterdam	Netherlands	Europe	C	3	0.9	Cfb	October-April
UTR	Utrecht	Netherlands	Europe	C	3	0.4	Cfb	October-April
DHA	Den Haag	Netherlands	Europe	C	3	0.5	Cfb	October-April
ROT	Rotterdam	Netherlands	Europe	C	3	0.6	Cfb	October-April
EIN	Eindhoven	Netherlands	Europe	C	3	0.2	Cfb	October-April
PAR	Paris	France	Europe	C	5	9.8	Cfb	October-March
BER	Berlin	Germany	Europe	C	34	3.8	Cfb	October-April
AUS	Augsburg	Germany	Europe	C	494	0.3	Cfb	October-March
MUN	Munich	Germany	Europe	C	519	1.6	Cfb	October-March
MIL	Milano	Italy	Europe	M	122	3.3	Cfa	15 October – 15 April
ROM	Rome	Italy	Europe	C	21	2.8	Csa	November – 15 April
NAP	Naples	Italy	Europe	C	100	1.0	Csa	15 November - March
BAR	Barcelona	Spain	Europe	M	13	5.1	Csa	November-March
MAD	Madrid	Spain	Europe	M	667	6.1	Csa/BSk	October-March
VAL	Valencia	Spain	Europe	M	16	1.6	Csa	November-March
SEV	Sevilla	Spain	Europe	M	11	1.3	Csa	November-March
ATH	Athens	Greece	Europe	M	70	3.7	Csa	November-April
NIC	Nicosia	Cyprus	Europe	M	220	0.3	BSh	November-March
GGA	Gr. Gauteng Reg.	South Africa	Africa	M	1500	15.5	Cwb	June-August
CAL	Calgary	Canada	North America	M	1084	1.6	Dfc	October-May
VAN	Vancouver	Canada	North America	M	4	2.6	Cfb	October-April
QUE	Quebec City	Canada	North America	M	74	0.8	Dfb	October-April
MON	Montreal	Canada	North America	M	77	4.1	Dfa/Dfb	October-April
OTT	Ottawa	Canada	North America	M	114	1.4	Dfb	October-April
HAL	Halifax	Canada	North America	M	242	0.4	Dfb	November - May
TOR	Toronto	Canada	North America	M	77	5.9	Dfa/Dfb	October-April
NYC	New York City	USA	North America	C	10	8.3	Dfa	October-May
LAN	Los Angeles	USA	North America	C	93	4.0	Csa	November-March
MEX	Mexico City M. A.	Mexico	North America	M	2250	23.6	Cwb	December-February
BOG	Bogota	Colombia	South America	M	2625	7.7	Cfb	no heating
QUI	Quito	Ecuador	South America	M	2835	2.8	Cfb/Cwb	no heating
LIM	Lima	Peru	South America	C	124	9.7	Bwh	June-September
RIO	Rio de Janeiro	Brazil	South America	C	20	6.7	Am	no heating
SAO	São Paulo	Brazil	South America	C	745	12.2	Cfa	no heating
SAN	Santiago	Chile	South America	M	500	7.2	Csb	May-August
SYD	Sydney	Australia	Australia	M	70	5.3	Cfa	May-September
MEL	Melbourne	Australia	Australia	M	31	5.1	Cfb	June-October

[1]Buildings are not provided with central heating in southern China and no heating season is prescribed and regulated.
[2]Heating period is not regulated. Hence, the definition is based on the coolest months of a year.

S2.3 Data sources and analysis protocols

S2.3.1 Air quality data sources

Table S2.3.1. The number of cities and sites (in brackets) analysed for each lockdown period and for each air pollutant species. Although data were analysed for a total of 63 cities and 540 sites, there was no city for which a complete dataset for all pollutants, lockdown phases and site types was available. The most comprehensive datasets were for NO_2, O_3 and PM, while NO had the lowest coverage.

Pollutant	Pre-lockdown	Partial lockdown	Full lockdown	Partial relaxation	Full relaxation
PM_{10}	52 (339)	28 (245)	50 (341)	49 (317)	30 (141)
$PM_{2.5}$	59 (343)	36 (236)	59 (349)	56 (298)	29 (118)
NO	46 (390)	34 (304)	44 (386)	43 (378)	20 (175)
NO_2	62 (529)	38 (391)	60 (529)	59 (495)	31 (236)
CO	49 (231)	31 (146)	48 (227)	46 (196)	24 (98)
SO_2	48 (244)	29 (188)	48 (246)	45 (223)	23 (84)
O_3	59 (394)	35 (268)	57 (393)	54 (308)	31 (176)

S2.3.3 Mobility data

Cities associated to each of the considered mobility data sources:

a) Apple driving: Greater Gauteng, Bengaluru, Chennai, Delhi, Hyderabad, Pune, London, Helsinki, Paris, Augsburg, Berlin, Munich, Athens, Naples Milano, Rome, Amsterdam, Eindhoven, Rotterdam, Den Haag, Utrecht, Barcelona, Madrid, Sevilla, Valencia, Stockholm, Calgary, Halifax, Montreal, Ottawa, Quebec, Toronto, Vancouver, Mexico City, Los Angeles, New York, City, Moscow, Melbourne and Sidney.
b) Google Retail: Chandigarh, Amritsar, Kolkata, Seoul, Tallinn, Tartu.
c) Waze: Rio de Janeiro, São Paulo, Santiago, Bogotá, Quito, Lima.
d) Baidu: Beijing, Chengdu, Guangzhou, Jinan, Shangai, Shenyang, Wuhan, Xian, Zhengshou.

Figure S2.3.1 presents the mobility variation index for each period of mobility (pre-, partial-, full-lockdown, partial relaxation and full relaxation) for all the cities from different mobility databases: Apple, Baidu, Google, and Waze. It is possible to observe that during the full-lockdown period they show coherence in the abatement of mobility.

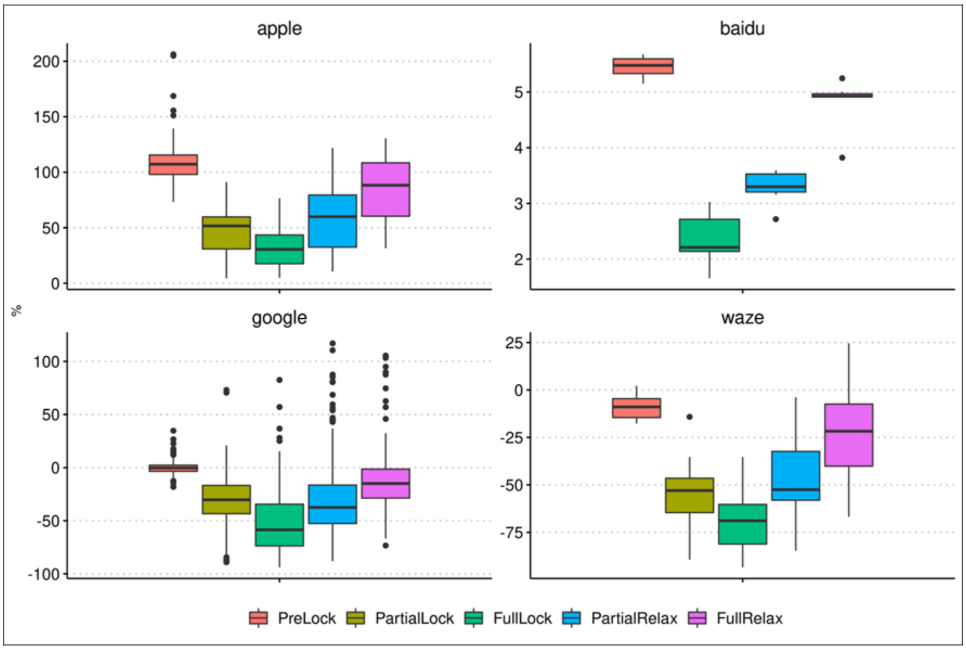

Figure S2.3.1. Average index for all the cities for mobility databases from Apple, Baidu, Google and Waze, for each period of analysis, pre-lockdown, partial lockdown, full lockdown, partial relaxation and full relaxation.

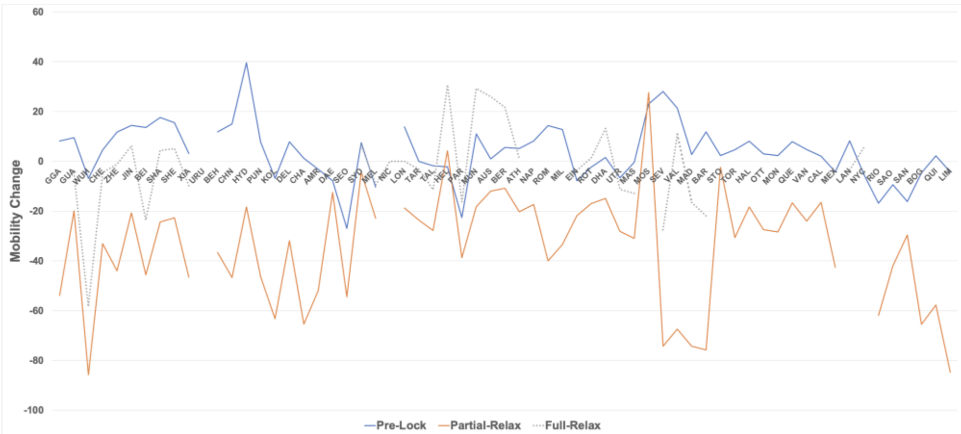

Figure S2.3.2. Mobility change during the periods classified as pre-lockdown, partial relaxation and full relaxation.

S3 Results analysis and discussion

S3.1 Changes in mobility and emissions

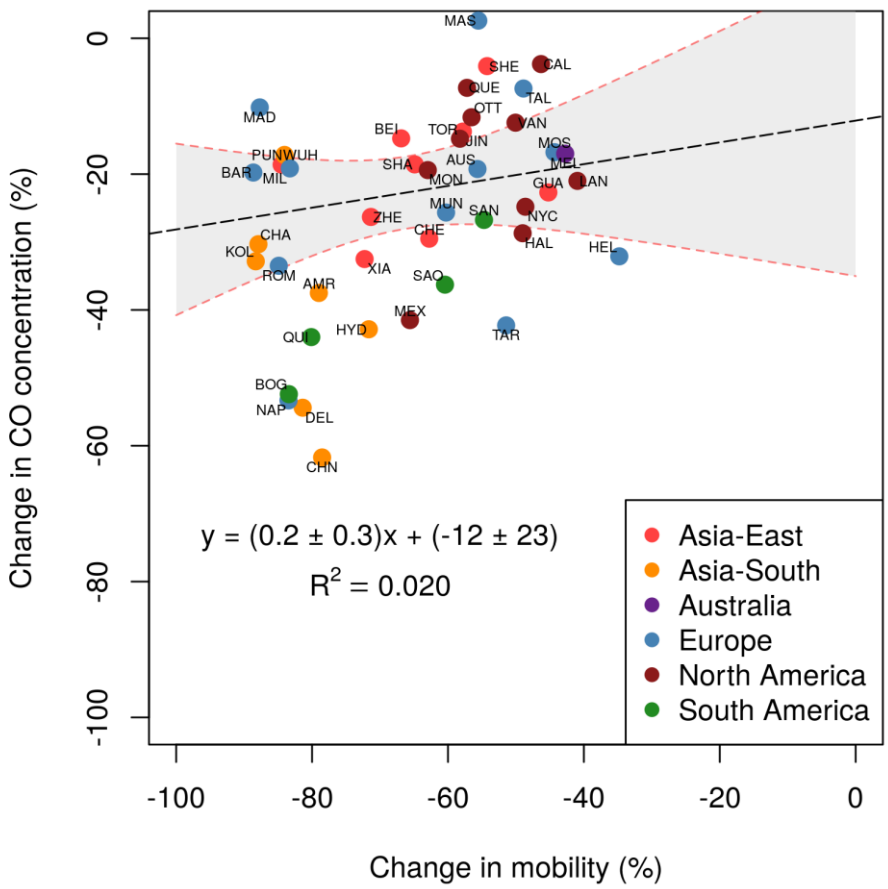

Figure S3.1.1. Linear regression fit (dashed line) and equation between CO and mobility percentage changes during full lockdown. The shaded area represents the 95% Confidence Interval.

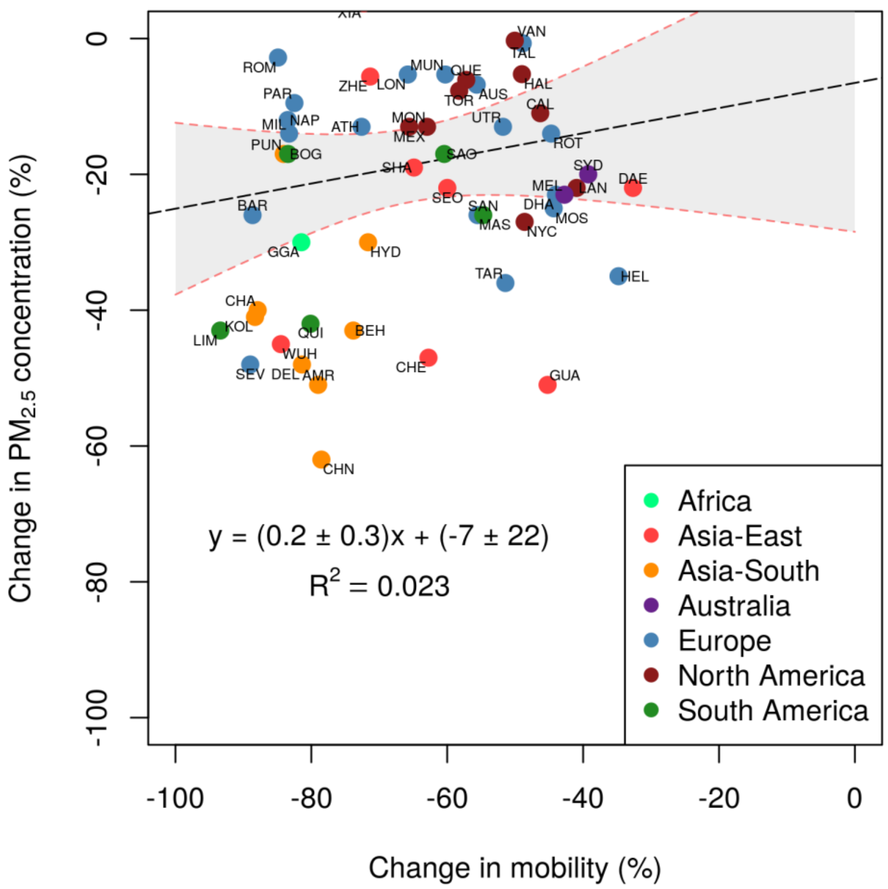

Figure S3.1.2. Linear regression fit (dashed line) and equation between PM2.5 and mobility percentage changes during full lockdown. The shaded area represents the 95% Confidence Interval.

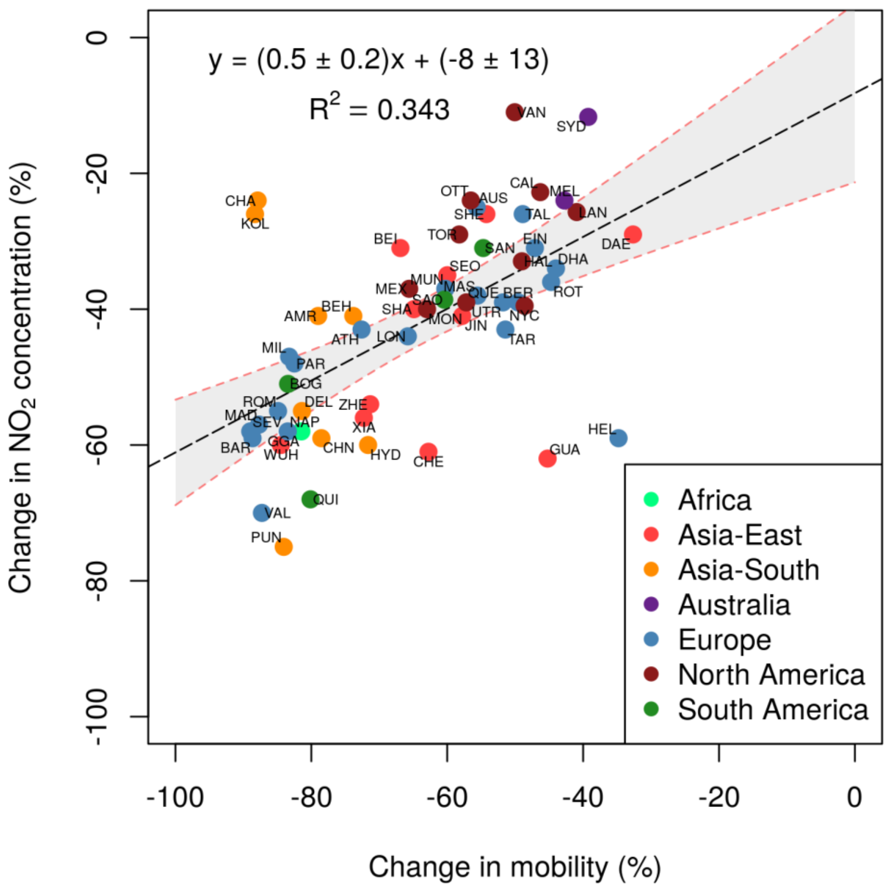

Figure S3.1.3. Linear regression fit (dashed line) and equation between NO2 and mobility percentage changes during full lockdown. The shaded area represents the 95% Confidence Interval.

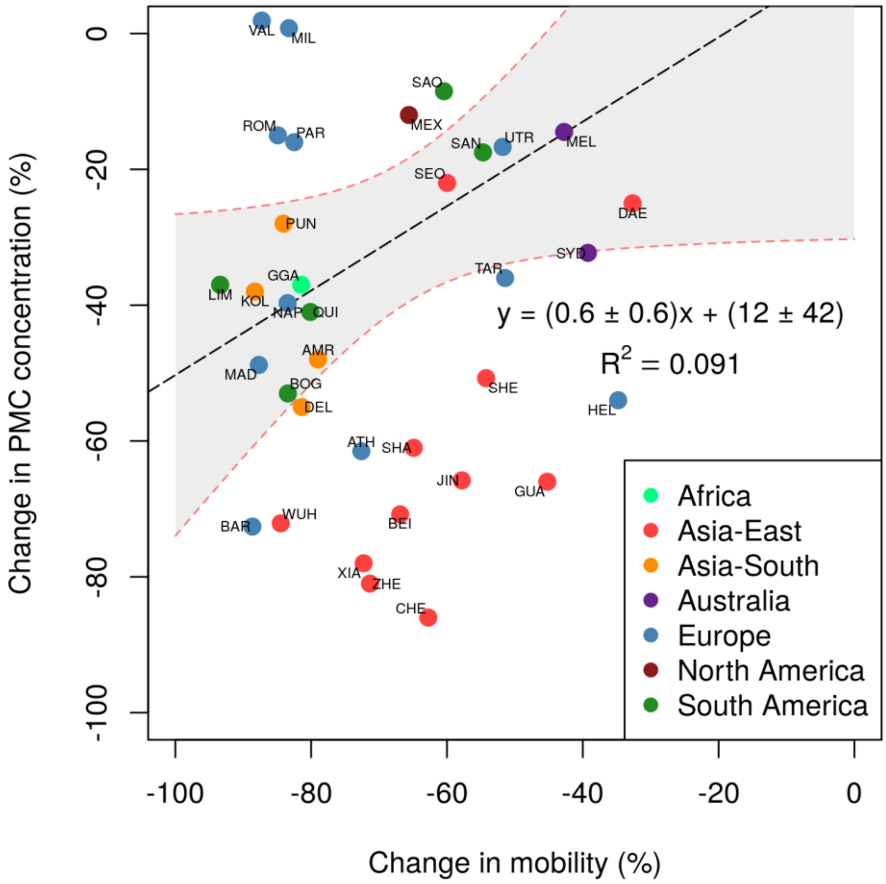

Figure S3.1.4. Linear regression fit (dashed line) and equation between PMC and mobility percentage changes during full lockdown. The shaded area represents the 95% Confidence Interval.

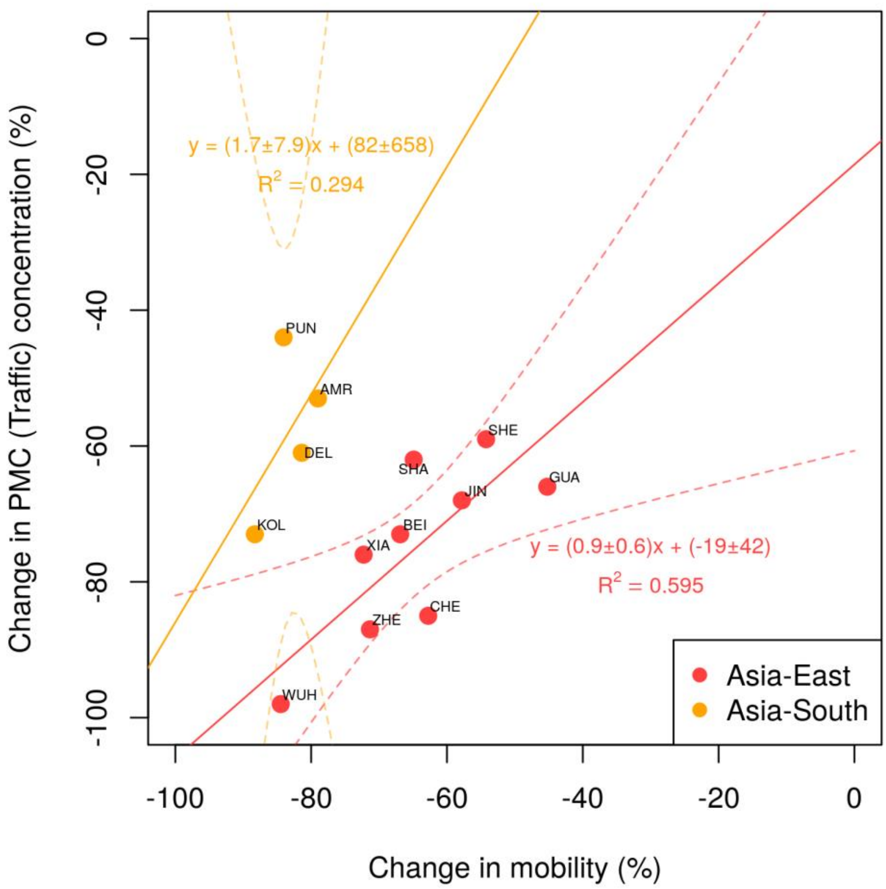

Figure S3.1.5. Linear regression fit (dashed line) and equation between PMC and mobility percentage changes during full lockdown for Indian and Chinese traffic sites. The dashed lines delimit the 95% Confidence Interval (Indian and Chinese cities only).

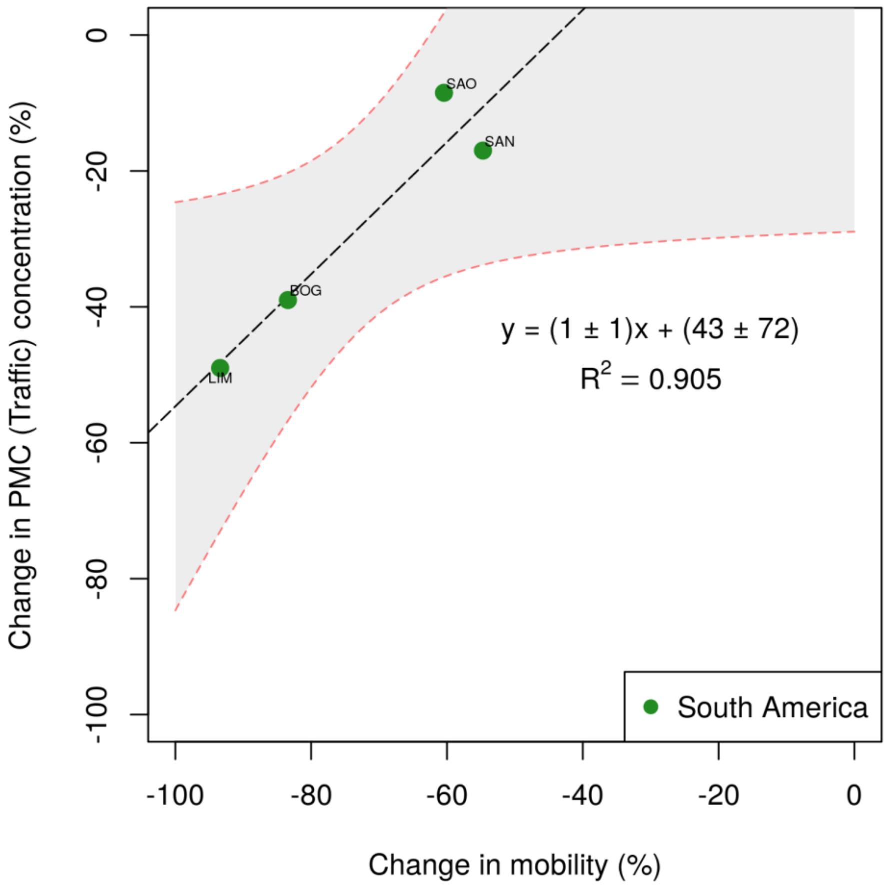

Figure S3.1.6. Linear regression fit (dashed line) and equation between PMC and mobility percentage changes during full lockdown for traffic sites in South America. The shaded area represents the 95% Confidence Interval.

S3.2 Implications of prevailing meteorology to changes in air quality

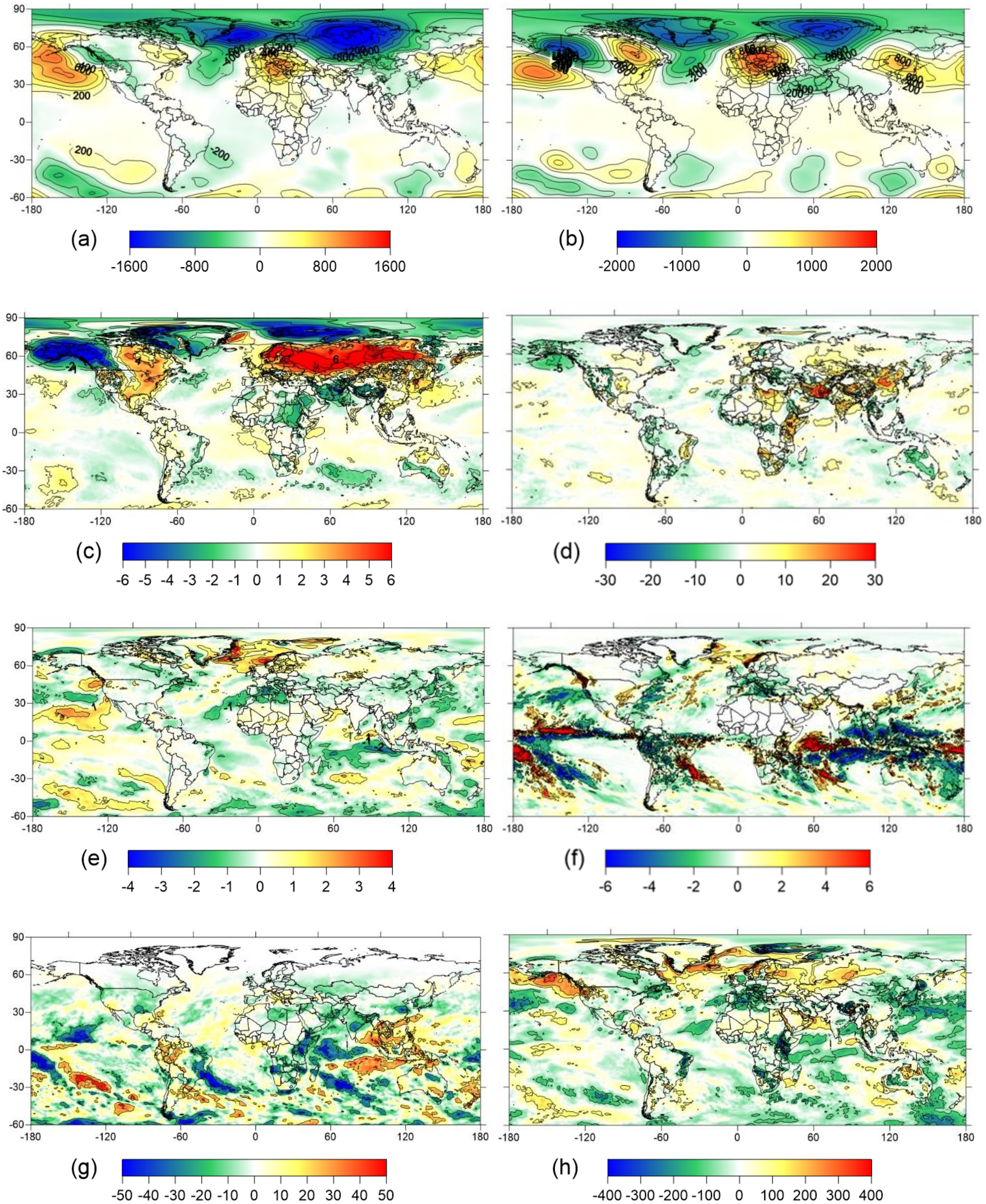

Figure S3.2.1. January 2020 anomalies with respect to 2015-2019 mean ERA5 reanalysis of (a) sea level pressure (Pa), (b) geopotential at 500 hPa (m^2/s^2), (c) 2-m temperature (K), (d) 2-m relative humidity (%), (e) 10-m wind speed (m/s), (f) precipitation rate (mm/day), (g) solar radiation (W/m^2), (h) boundary layer depth (m).

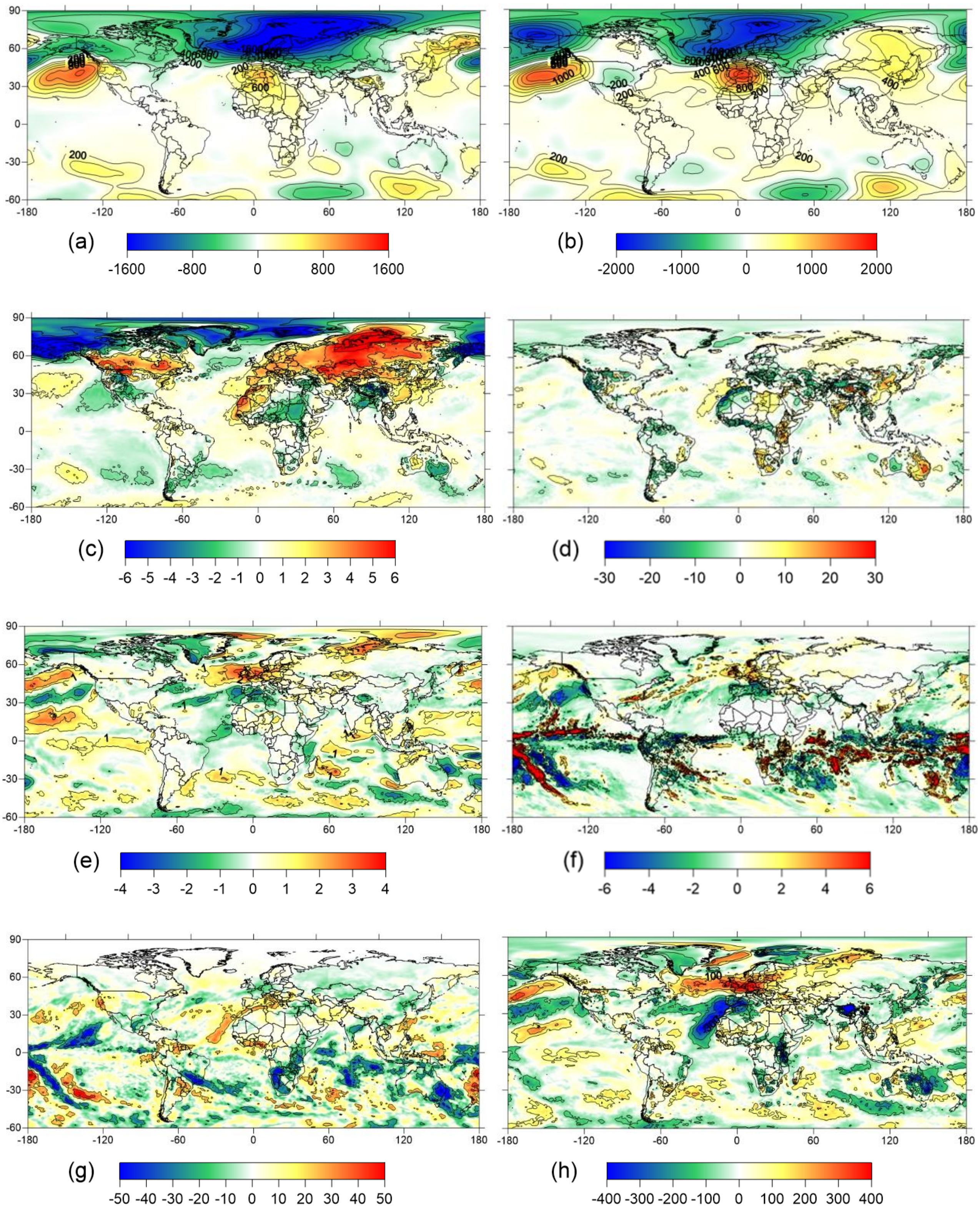

Figure S3.2.2. February 2020 anomalies with respect to 2015-2019 mean ERA5 reanalysis of (a) sea level pressure (Pa), (b) geopotential at 500 hPa (m^2/s^2), (c) 2-m temperature (K), (d) 2-m relative humidity (%), (e) 10-m wind speed (m/s), (f) precipitation rate (mm/day), (g) solar radiation (W/m^2), (h) boundary layer depth (m).

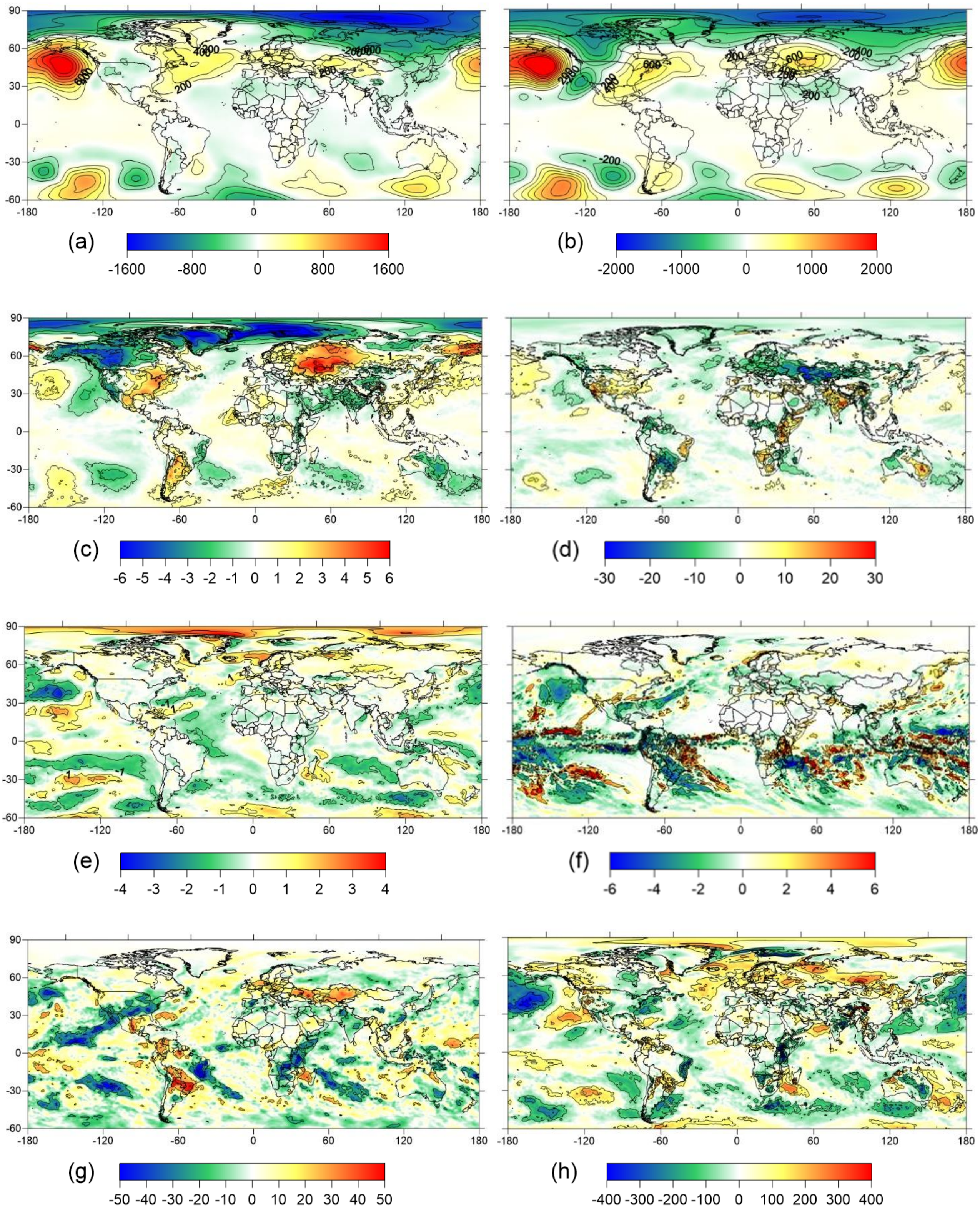

Figure S3.2.3. March 2020 anomalies with respect to 2015-2019 mean ERA5 reanalysis of (a) sea level pressure (Pa), (b) geopotential at 500 hPa (m^2/s^2), (c) 2-m temperature (K), (d) 2-m relative humidity (%), (e) 10m wind speed (m/s), (f) precipitation rate (mm/day), (g) solar radiation (W/m^2), (h) boundary layer depth (m).

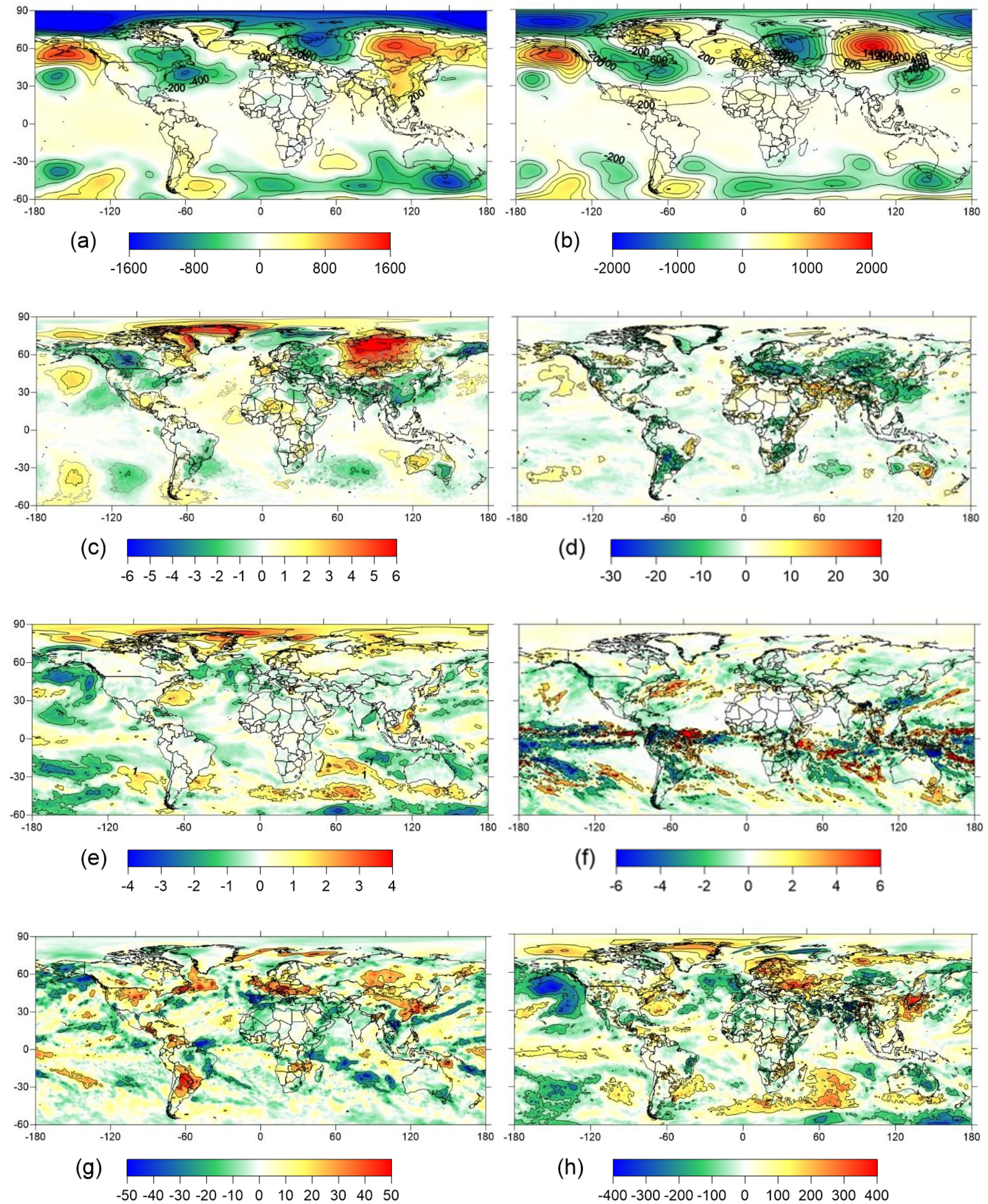

Figure S3.2.4. April 2020 anomalies with respect to 2015-2019 mean ERA5 reanalysis of (a) sea level pressure (Pa), (b) geopotential at 500 hPa (m^2/s^2), (c) 2m temperature (K), (d) 2m relative humidity (%), (e) 10m wind speed (m/s), (f) precipitation rate (mm/day), (g) solar radiation (W/m^2), (h) boundary layer depth (m).

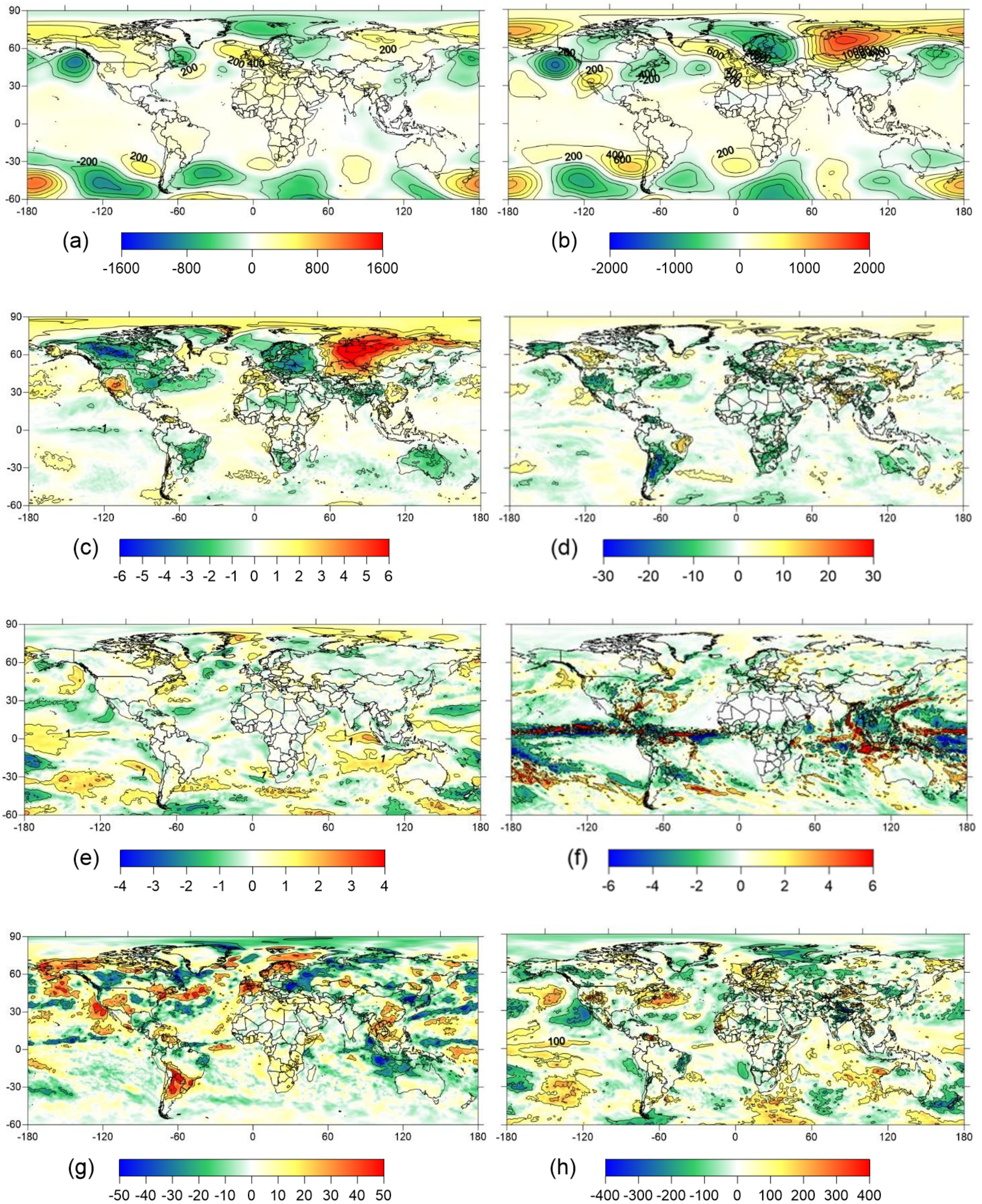

Figure S3.2.5. May 2020 anomalies with respect to 2015-2019 mean ERA5 reanalysis of (a) sea level pressure (Pa), (b) geopotential at 500 hPa (m^2/s^2), (c) 2-m temperature (K), (d) 2-m relative humidity (%), (e) 10m wind speed (m/s), (f) precipitation rate (mm/day), (g) solar radiation (W/m^2), (h) boundary layer depth (m).

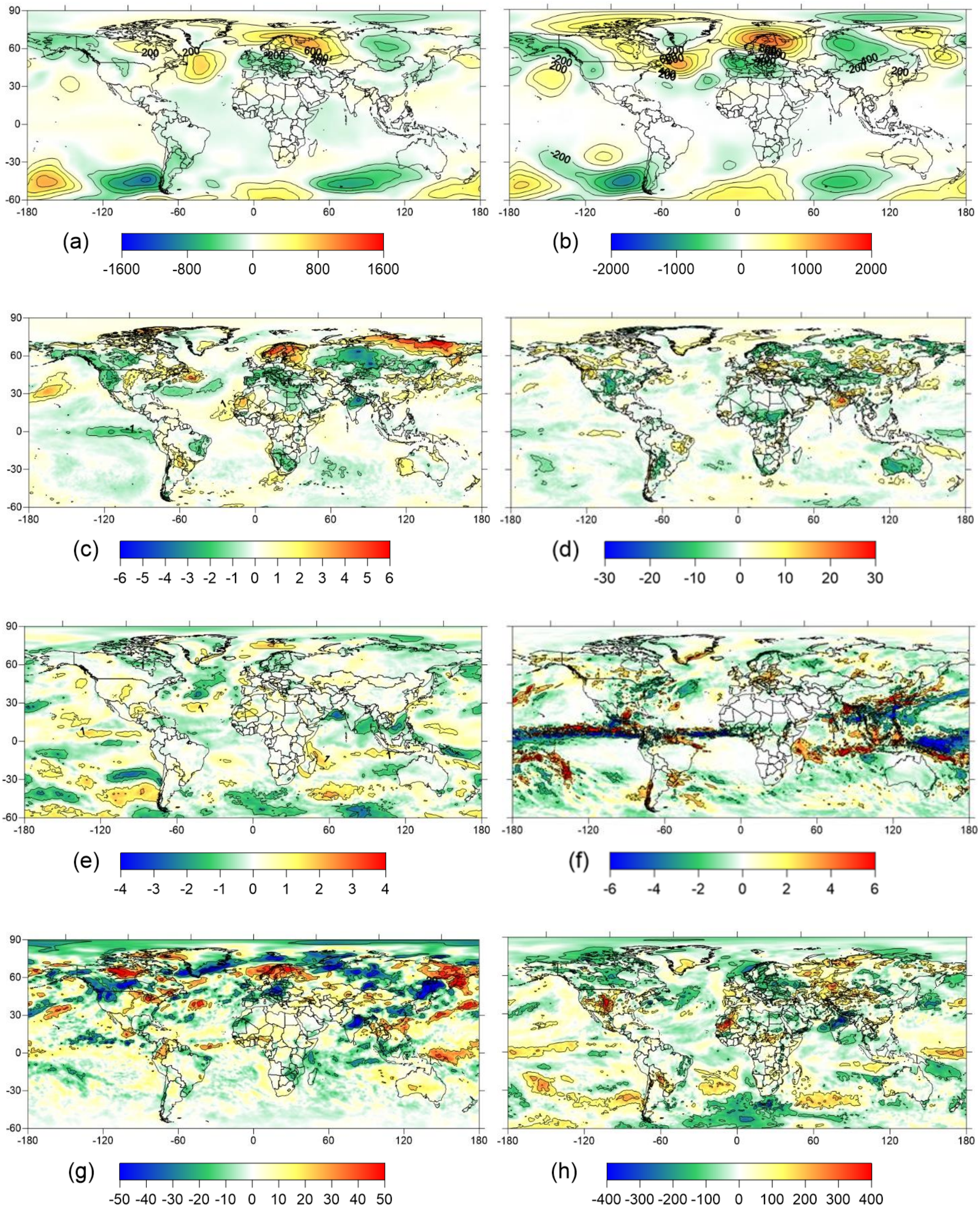

Figure S3.2.6. June 2020 anomalies with respect to 2015-2019 mean ERA5 reanalysis of (a) sea level pressure (Pa), (b) geopotential at 500 hPa (m^2/s^2), (c) 2-m temperature (K), (d) 2-m relative humidity (%), (e) 10m wind speed (m/s), (f) precipitation rate (mm/day), (g) solar radiation (W/m^2), (h) boundary layer depth (m).

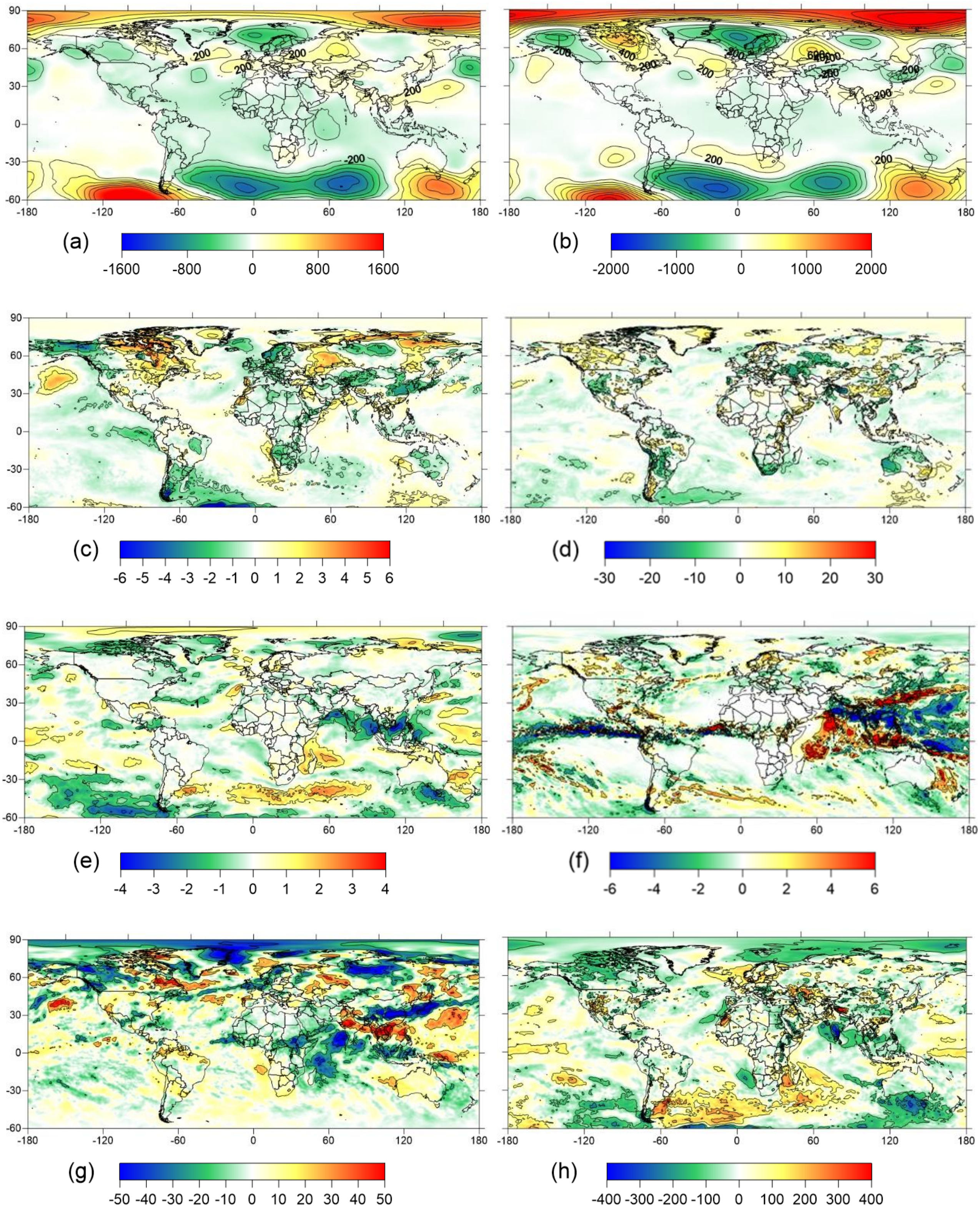

Figure S3.2.7. July 2020 anomalies with respect to 2015-2019 mean ERA5 reanalysis of (a) sea level pressure (Pa), (b) geopotential at 500 hPa (m^2/s^2), (c) 2-m temperature (K), (d) 2-m relative humidity (%), (e) 10m wind speed (m/s), (f) precipitation rate (mm/day), (g) solar radiation (W/m^2), (h) boundary layer depth (m).

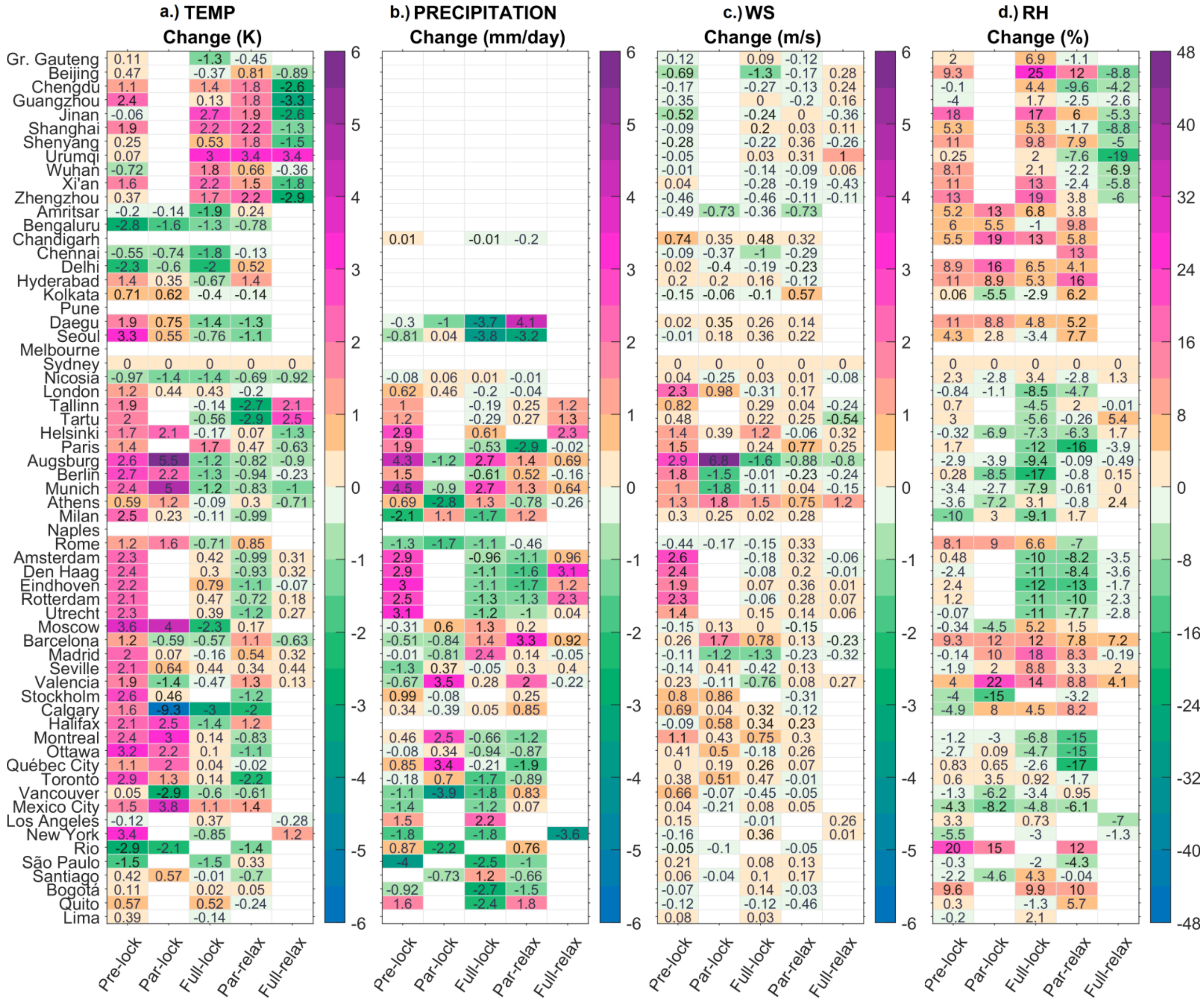

Figure S3.2.8. Mean observed in situ anomalies during the different COVID-19 lockdown phases compared with their corresponding periods in 2015-2019, (a) 2-m temperature (K), (b) precipitation rate (mm/day), (c) 10-m wind speed (m/s), (d) 2-m relative humidity (%).

S3.3 Air quality and long-range transport of pollutants

Table S3.3.1. Air pollution episodes and atypical anticyclonic conditions affecting cities of interest during the lockdown periods during 2020.

City	Event	Period
Seville, Madrid, Valencia, Barcelona	LRT Dust	15-20 March
Naples, Rome	LRT Dust	18-20 April
Milan	LRT Dust	27-29 March
Athens	LRT Dust	7-9 and 23 March; 3-5 April
Nicosia	LRT Dust	5-7, 13-15 and 24 March;-5 and 21-23 April
Zhengzhou	LRT Dust	24 January, 4 February, 18 March
Xi'an, Beijing and Jinan	LRT Dust	18 March
Several European regions (e.g. Amsterdam, Ausburg, Munich, Paris)	LRT Dust	16-30 March
Moscow	LRT biomass burning	29-31 March, 14-15 April
Mexico city	LRT biomass burning	26 April – 19 May
Bogotá	LRT biomass burning	2 February – 1 May
All Asian cities except Urumqi, Xi'an and Hyderabad	LRT biomass burning	During different lockdown periods
Vancouver	Atypical anticyclonic conditions	February to April
Halifax	Atypical anticyclonic conditions	March
Seville, Madrid, Valencia, Barcelona	Atypical anticyclonic conditions	February
Shenyang, Beijing, Seoul, Daegu	Atypical anticyclonic conditions	January, February

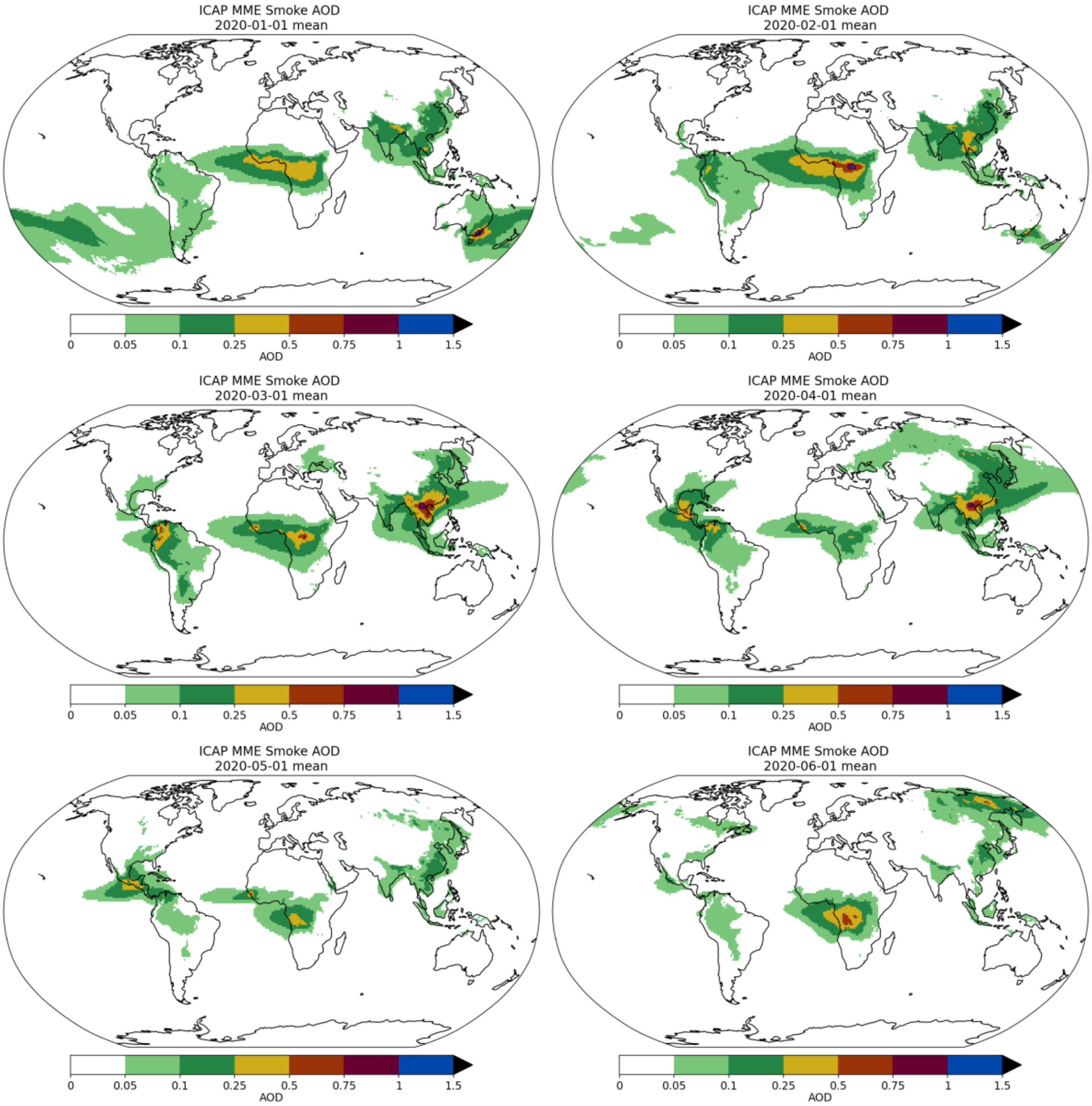

Figure S3.3.1. Monthly means (January to June 2020) of the ICAP/MME **smoke** AOD

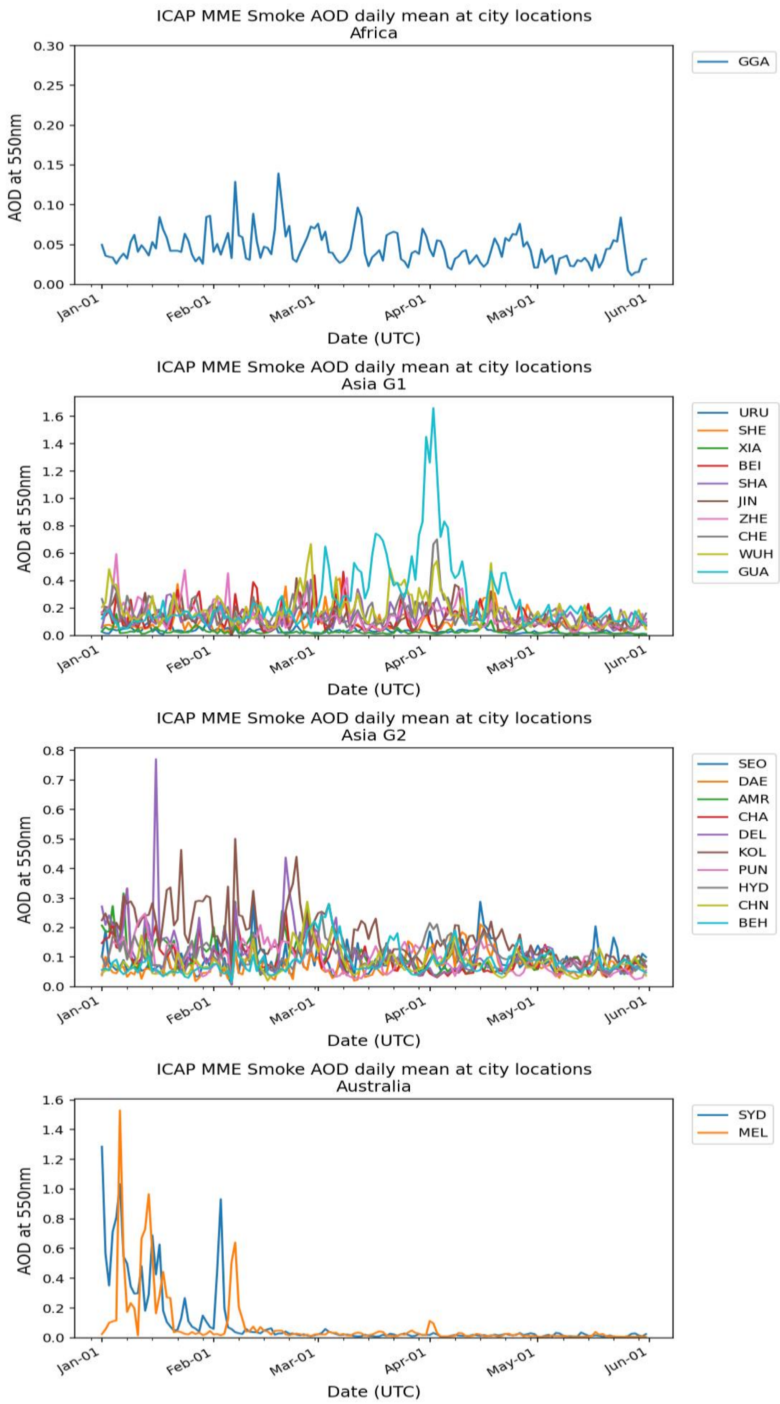

Figure S3.3.2. Time series (January to June 2020) of ICAP/MME daily means of the **smoke** AOD over considered cities in Africa, Asia and Australia. The three-letter city acronyms are defined in Table S2.1.1.

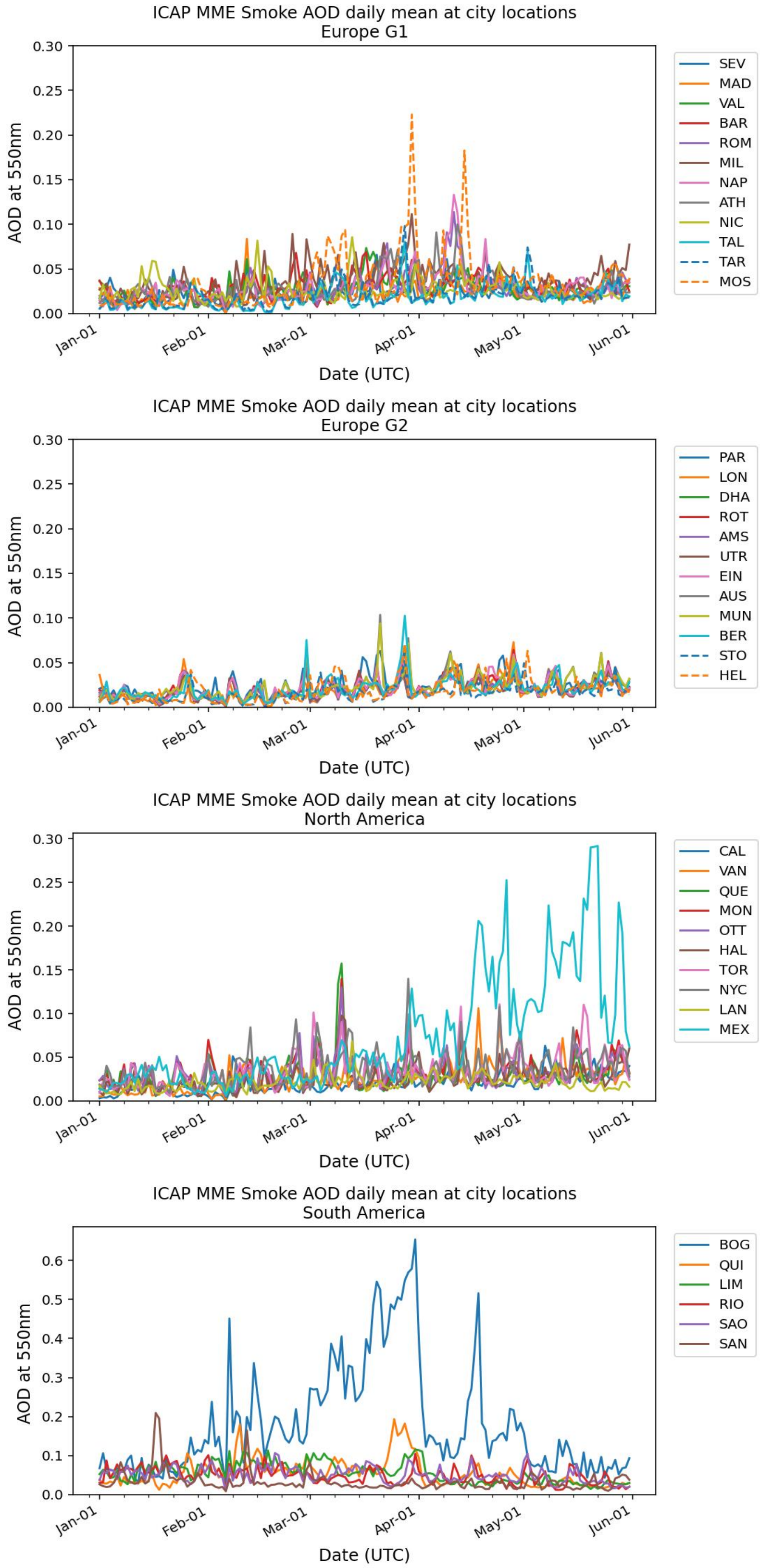

Figure S3.3.3. Time series (January to June 2020) of ICAP/MME daily means of the **smoke** AOD over considered cities in Europe, North and South America. The three-letter city acronyms are defined in Table S2.1.1.

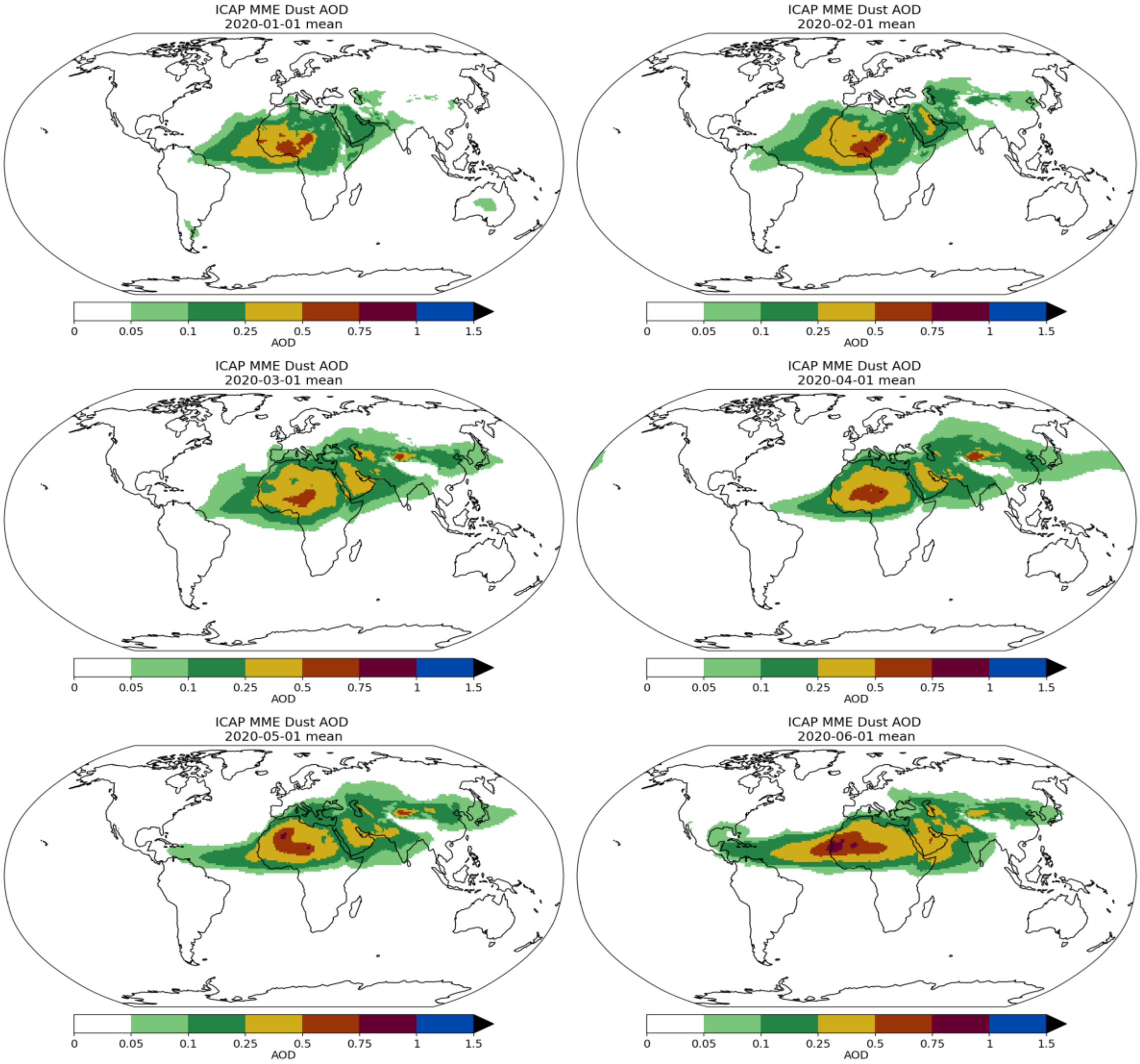

Figure S3.3.4. Monthly means (January to June 2020) of the ICAP/MME **Dust** AOD.

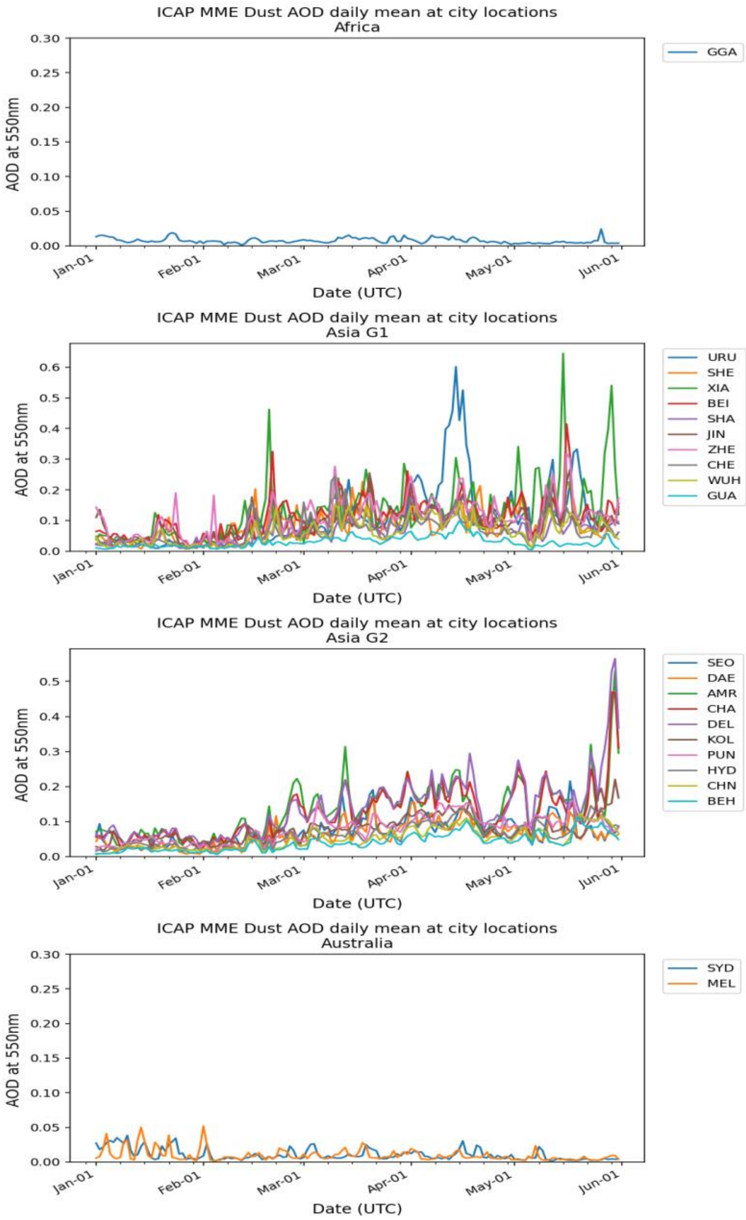

Figure S3.3.5. Time series (January to June 2020) of ICAP/MME daily means of the **Dust** AOD over considered cities in Africa, Asia and Australia. The three-letter city acronyms are defined in Table S2.1.1.

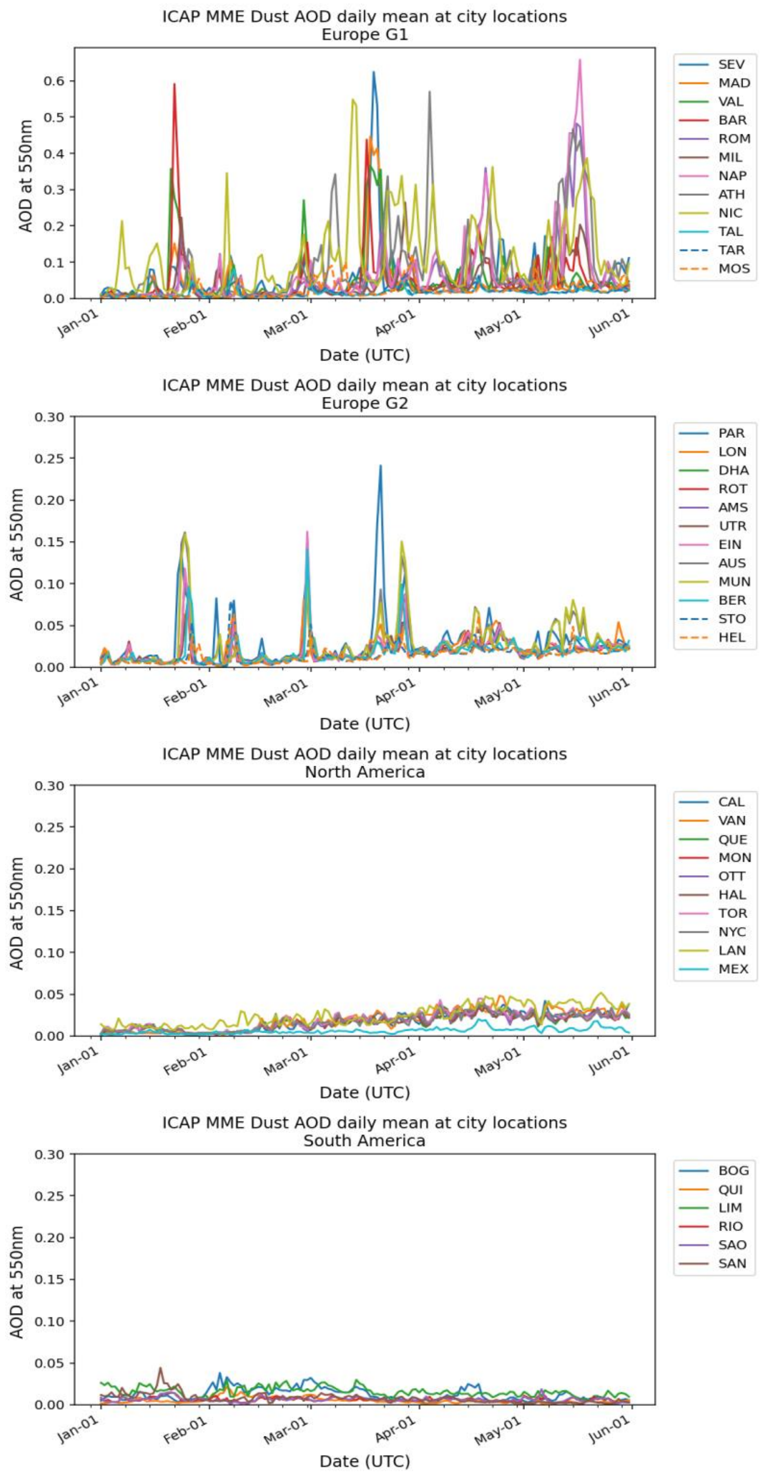

Figure S3.3.6. Time series (January to June 2020) of ICAP/MME daily means of the **Dust** AOD over considered cities in Europe, North and South America. The three-letter city acronyms are defined in Table S2.1.1.

S3.4 Changes in air pollutant concentrations during the lockdown periods

S3.4.1 Carbon monoxide concentrations for 2015–2019

On a global scale, CO concentrations were the highest in Asia in 2015–2019 (see Figure S3.4.17a). The Indian and Chinese cities recorded the highest concentrations (750–4000 µg/m^3), followed by the South American and some Italian cities (600–1200 µg/m^3). The Canadian, US, Australian and rest of the European cities recorded the lowest concentrations (200–400 µg/m^3).

Strong inter-annual CO variations were observed in many countries, due to a combination of changes in emissions, meteorology and chemistry seasonal cycles (e.g., Sheel et al., 2014; Rozente et al., 2017). Cities in India and China recorded marked decreasing trends (up to -38%) for 2015–2019, probably following the trends described by Zheng et al*.* (2018) derived from continuous emission control policies. Decreasing trends were also observed in Mexico, Australia, some south-eastern Canadian cities (Montreal, Quebec and Ottawa), and Europe (Estonia, Finland, Italy, coastal cities of Spain and France). For a few cities, such as Madrid and Amsterdam, a 30% increase was observed over the period.

A pronounced seasonal pattern was evident in most NH cities, where CO concentrations decreased from the pre-lockdown to the relaxation periods (Figure S3.4.17b), which we believe to have been driven by both meteorological changes from winter to summer and by energy use (e.g., mobility and indoor heating). An opposite pattern was observed in the SH, especially in the Andean cities (Santiago, Quito and Bogotá) with maximum CO concentrations in the full lockdown period, coinciding with the winter season, with Santiago showing a nearly three-fold increase. Mendez-Espinosa et al. (2019), using a 10-year climatology of trace pollutants, have shown that CO peaks occur in February and March in Bogotá, associated with biomass burning and stagnant atmospheric conditions.

S3.4.2 Relative CO changes by type of environment

The available CO data were predominantly from traffic and urban background sites, except for China (see Figure S3.4.17e). In most American, Indian and European cities, the decreases during the lockdown were most likely dominated by the reduction in traffic emissions, since negative CO anomalies were higher at traffic sites. Conversely, CO variations in several Chinese cities showed a more homogeneous spatial pattern across rural, industrial and urban background sites, suggesting that all different anthropogenic activities affected the CO concentrations. Seville and Madrid showed the largest increases at traffic and rural sites, respectively, but the signal may have been affected by domestic biomass burning because the sites are located within residential areas.

S3.4.3 Sulphur dioxide concentrations for 2015–2019

SO_2 showed variability on a worldwide scale (Figure S3.4.23), with higher concentrations in Asia than in other regions. The Chinese and Indian cities registered the highest mean SO_2 concentrations during the corresponding lockdown periods in BAU periods of 2015-2019 (from 10.7 to 78.5 µg/m^3 and from 7.3 to 15.9 µg/m^3, respectively). Other cities exhibited lower SO_2 concentrations, with all but Mexico City and Madrid having mean concentrations in BAU lower than 6 µg/m^3, with the lowest values (0.38-1.6 µg/m^3) in Estonian cities. Strong inter-annual SO_2 variations were evident in most countries in 2015–2019. A decreasing trend from 2015 to 2019 was seen in China, South Korea, Europe (France, Estonia, Italy and the Netherlands), Mexico, US, Brazil, and Ecuador. Some countries, however, showed either no changes or increasing trends, including India, Australia and Europe (Cyprus, Finland, Spain except Barcelona), and the cities of Halifax and Bogotá.

Temporal variabilities in SO_2 concentrations were observed for most cities from 2015 to 2019 (Figure S3.4.23). In Asian cities (except Chennai, Delhi and Hyderabad), the decreases were prominent from the pre-lockdown to the relaxation periods. As the temperature increased from pre-lockdown to full lockdown, a reduction in residential heating emissions may have partly contributed to the temporal decrease in SO_2 (Liu et al., 2016; Zhai et al., 2019). In other NH cities, such as those in Europe and North America (except for Naples, Toronto, and Vancouver), decreases were also large (up to 64%). Conversely, in the SH, the SO_2 concentrations increased which may be attributed to the winter heating emission and the influence of the Amazonian fires (Buchholz et al., 2018). Besides, enhanced oxidizing capacity can promote the formation of sulfate by oxidizing SO_2, and increases in OX can be understood as enhancements in the abundance of oxidants (e.g., OH) (Lee et al., 2020; Shen et al., 2021). Hence, increased seasonal OX in most NH cities while decreases in SH cities (not shown) can be another cause for the opposite temporal variabilities in worldwide SO_2 levels.

S3.4.4 Relative changes during full lockdown period by type of environment

Because most SO_2 monitoring stations were either traffic or urban types (Figure S3.4.23e), the SO_2 decreases during the lockdown compared to the 2015–2019 means at traffic sites were prominent in China, some southern European and American cities (most saw decreases larger than -40%) and two of the three Indian cities (Delhi and Hyderabad). In the case of Chennai, there was an increase of 20% at the traffic site but a significant decrease of 66% at the industrial station which requires further investigation. Chinese, some northern European and southern American urban background sites also showed large decreases, while Naples, Calgary, and Ottawa had increases at urban background sites (6.2 to 29%). All of the industrial stations showed reductions during 2020 compared to BAU. For rural stations only Valencia showed an increase (+9.9%) for 2020. As mentioned above, interpreting isolated instances is difficult for SO_2 but overall, there were decreasing trends globally over the 2020 lockdown periods compared to BAU at most station types.

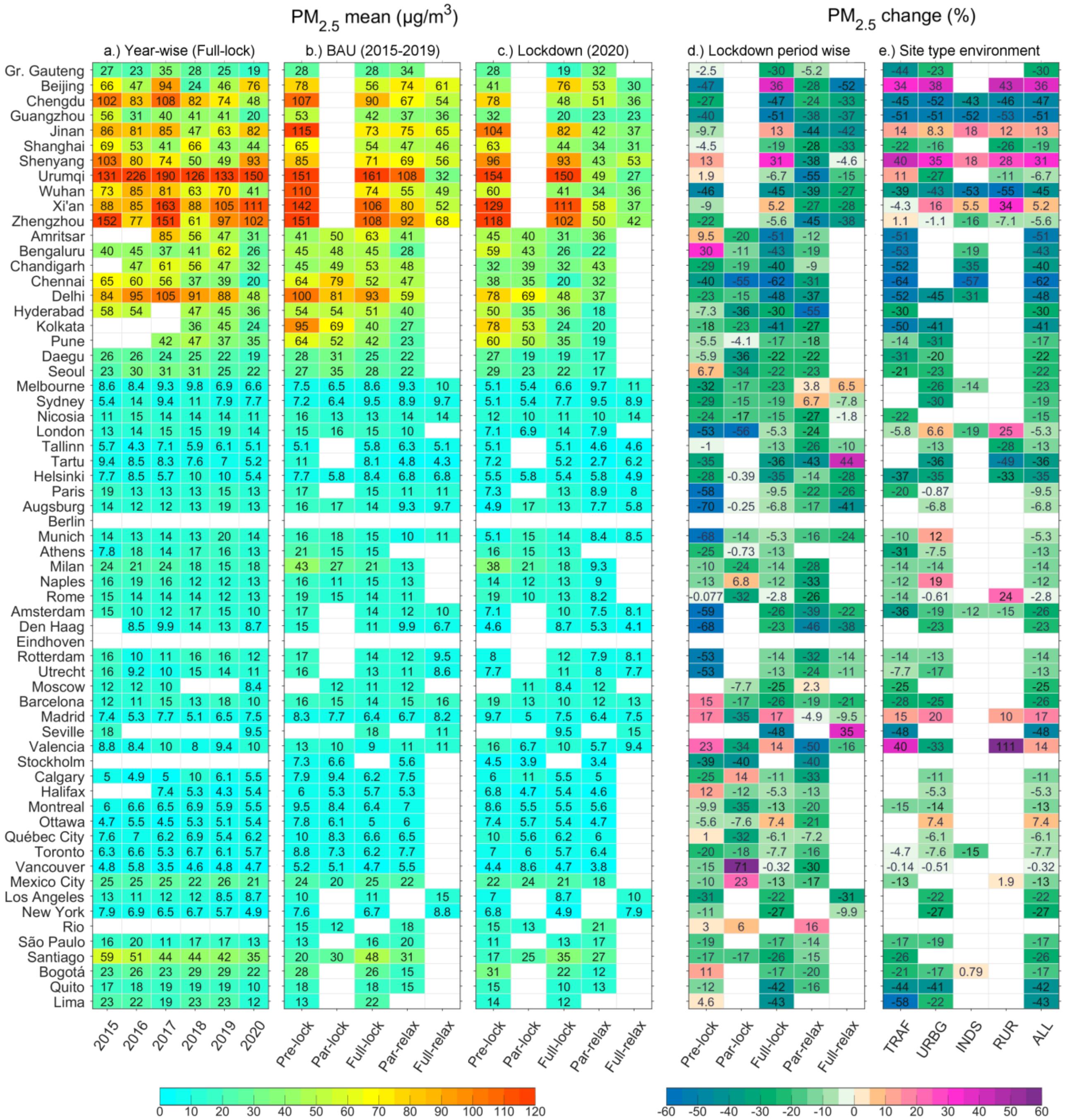

Figure S3.4.1. Observed concentrations (μg/m^3) and percentage changes in $PM_{2.5}$ (a) Mean concentrations for the full lockdown period for years 2015 to 2020, (b) Mean concentrations for different matching lockdown periods during BAU, (c) Observed mean concentrations during 2020 for different lockdown periods, (d) Percentage changes observed for different lockdown periods, and (e) Percentage changes observed for full lockdown in different environments.

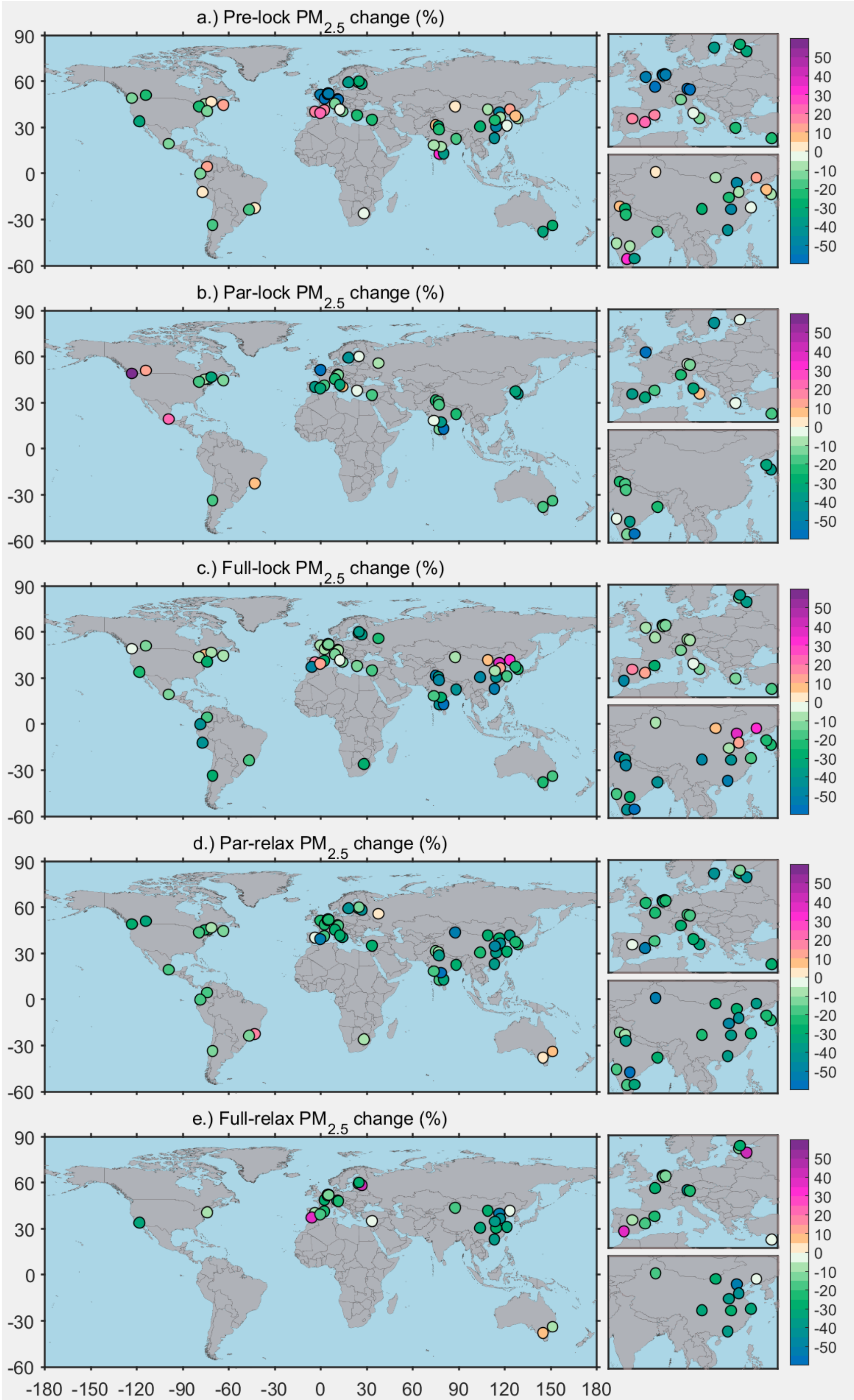

Figure S3.4.2. Observed percentage change in $PM_{2.5}$ on global map for (a) pre-lockdown, (b) partial lockdown, (c) full lockdown, (d) partial relaxation, and (e) full relaxation. The small sub-panel maps show zooms of European and Asian countries.

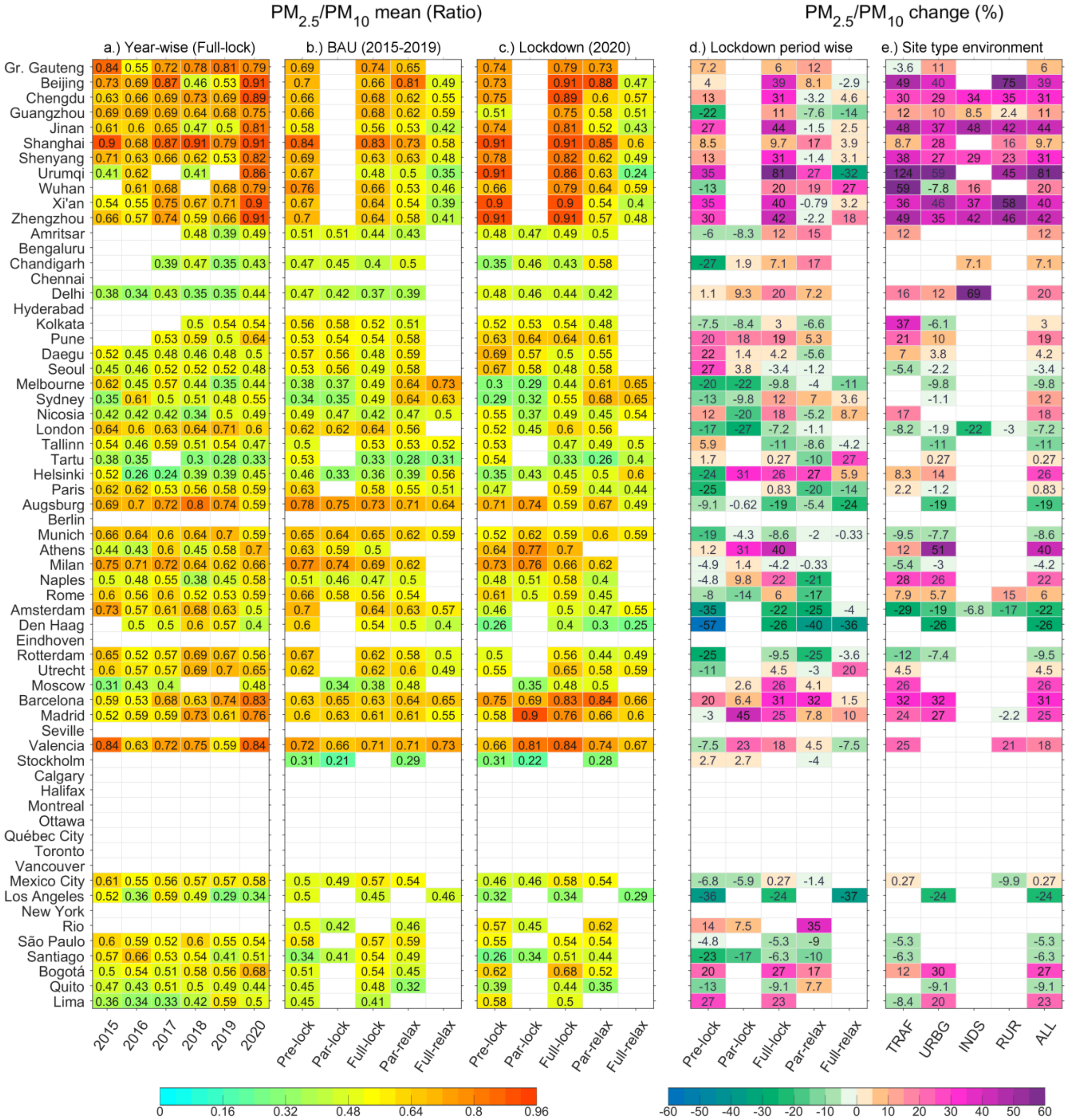

Figure S3.4.3. Observed concentration ratios and percentage changes in $PM_{2.5}/PM_{10}$ concentration ratios (a) Mean concentration ratios for the equivalent full lockdown period for each year from 2015 to 2020, (b) Mean concentration ratios for different equivalent lockdown periods during BAU (2015-2019), (c) Observed mean concentration ratios during 2020 for different lockdown periods, (d) Percentage changes observed for different lockdown periods, and (e) Percentage changes observed for full lockdown in different environments.

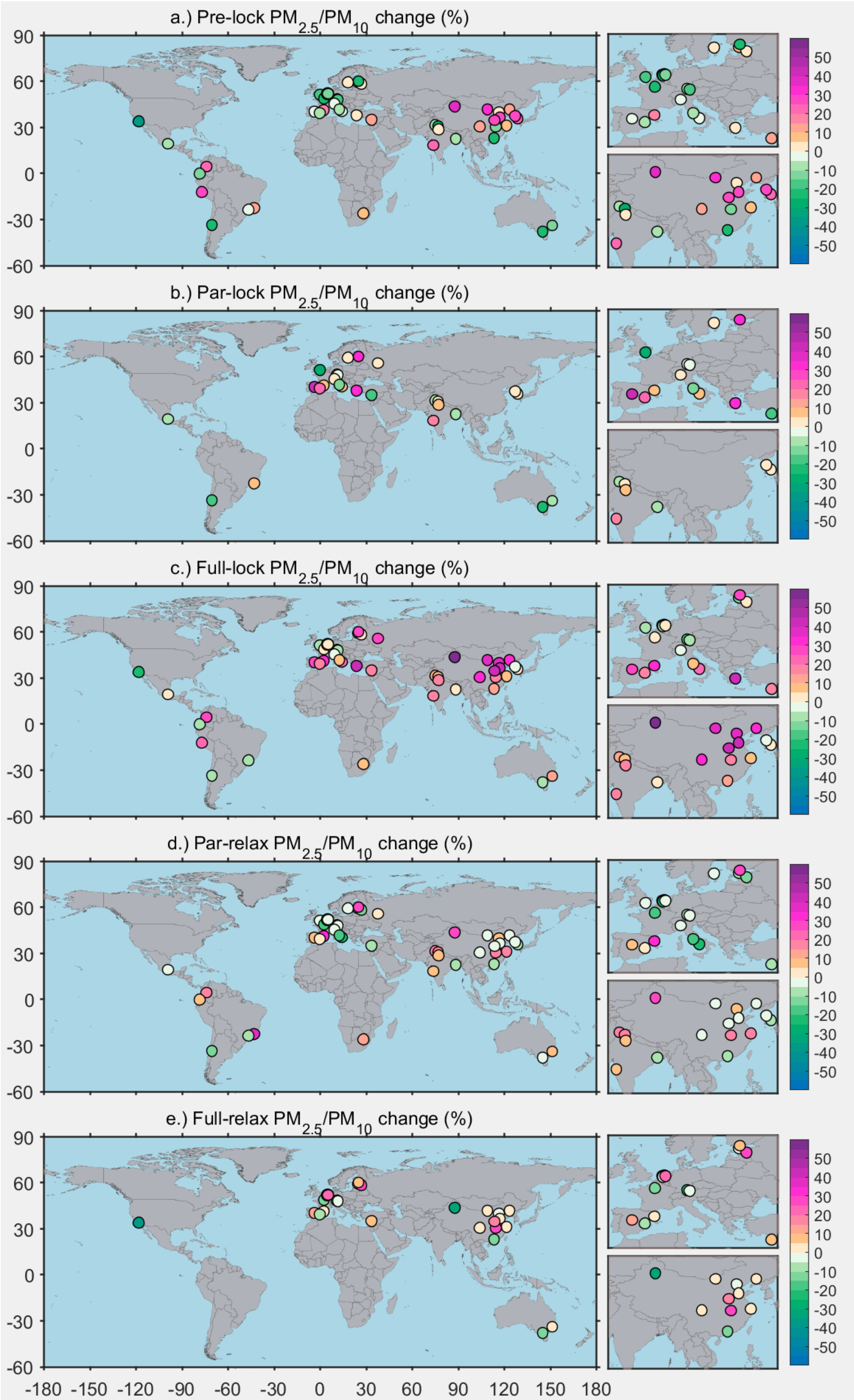

Figure S3.4.4. Observed percentage changes in $PM_{2.5}/PM_{10}$ on global maps for (a) pre-lockdown, (b) partial lockdown, (c) full lockdown, (d) partial relaxation, and (e) full relaxation. The small sub-panel maps show zoom of European and Asian countries.

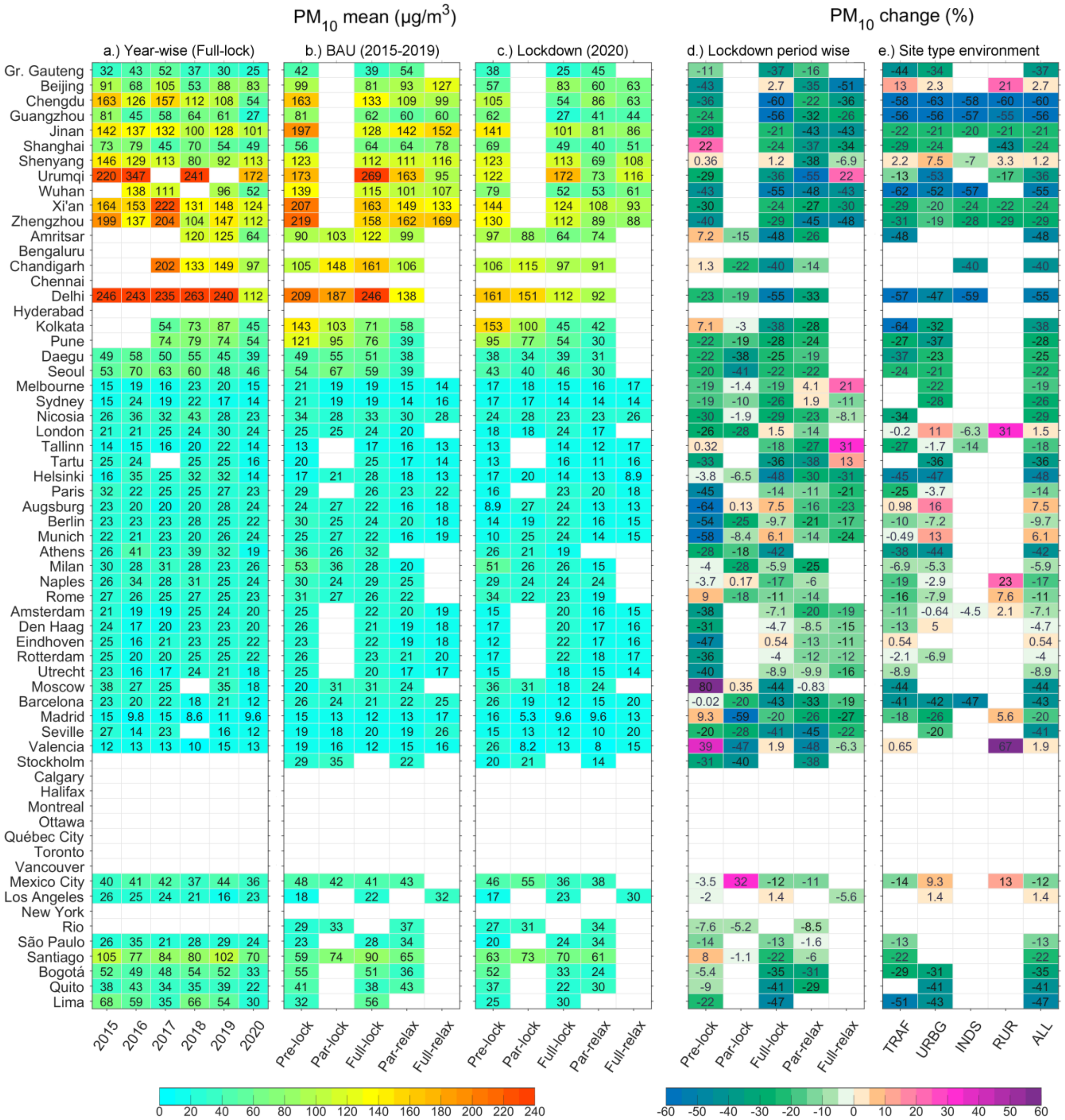

Figure S3.4.5. Observed concentrations (µg/m^3) and percentage changes in PM_{10} (a) Mean concentrations for the equivalent full lockdown period for each year from 2015 to 2020, (b) Mean concentrations for different equivalent lockdown periods during BAU (2015-2019), (c) Observed mean concentrations during 2020 for different lockdown periods, (d) Percentage changes observed for different lockdown periods, and (e) Percentage changes observed for full lockdown in different environments.

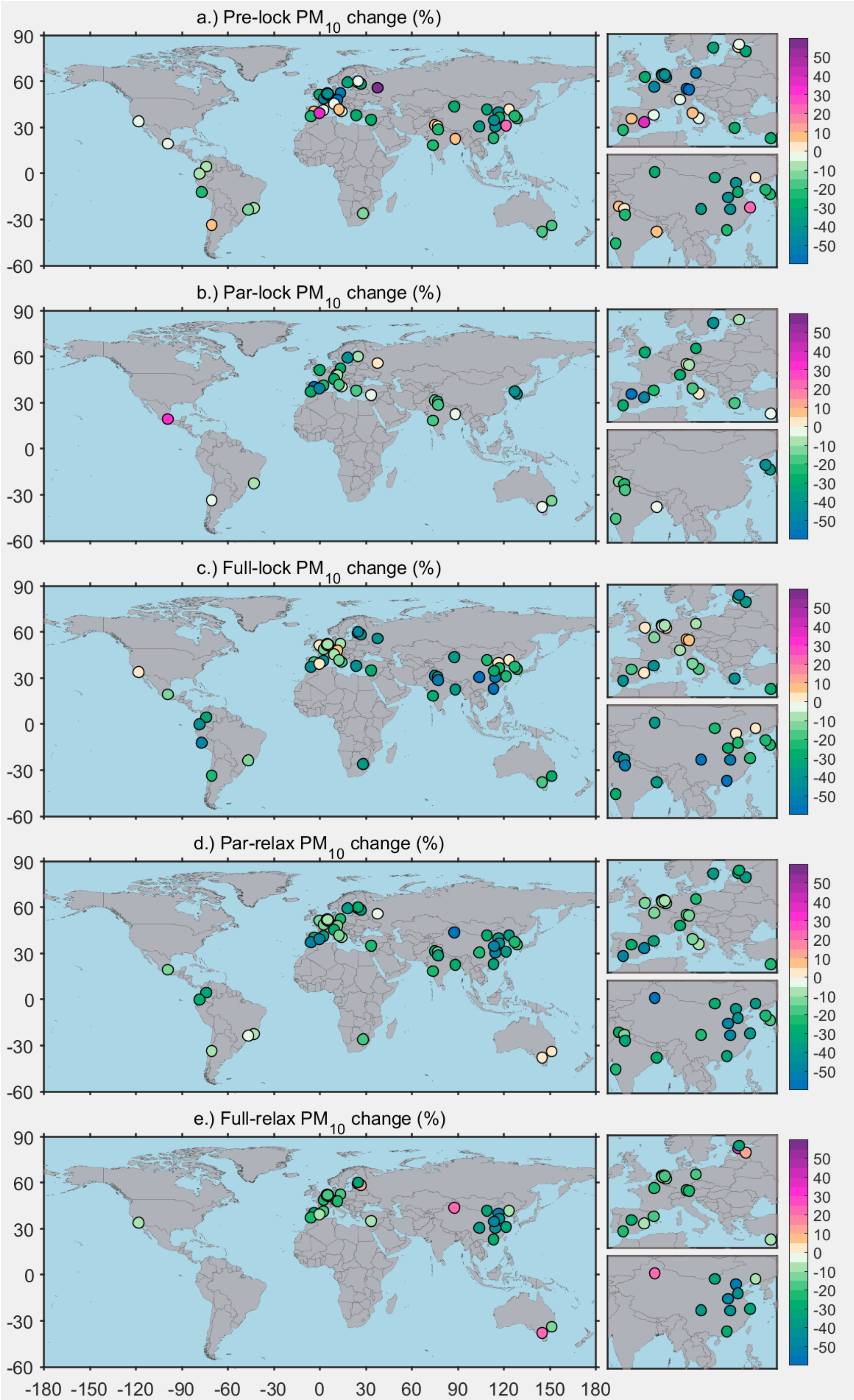

Figure S3.4.6. Observed percentage changes in PM_{10} on global maps for (a) pre-lockdown, (b) partial lockdown, (c) full lockdown, (d) partial relaxation, and (e) full relaxation. The small sub-panel maps show zoom of European and Asian countries.

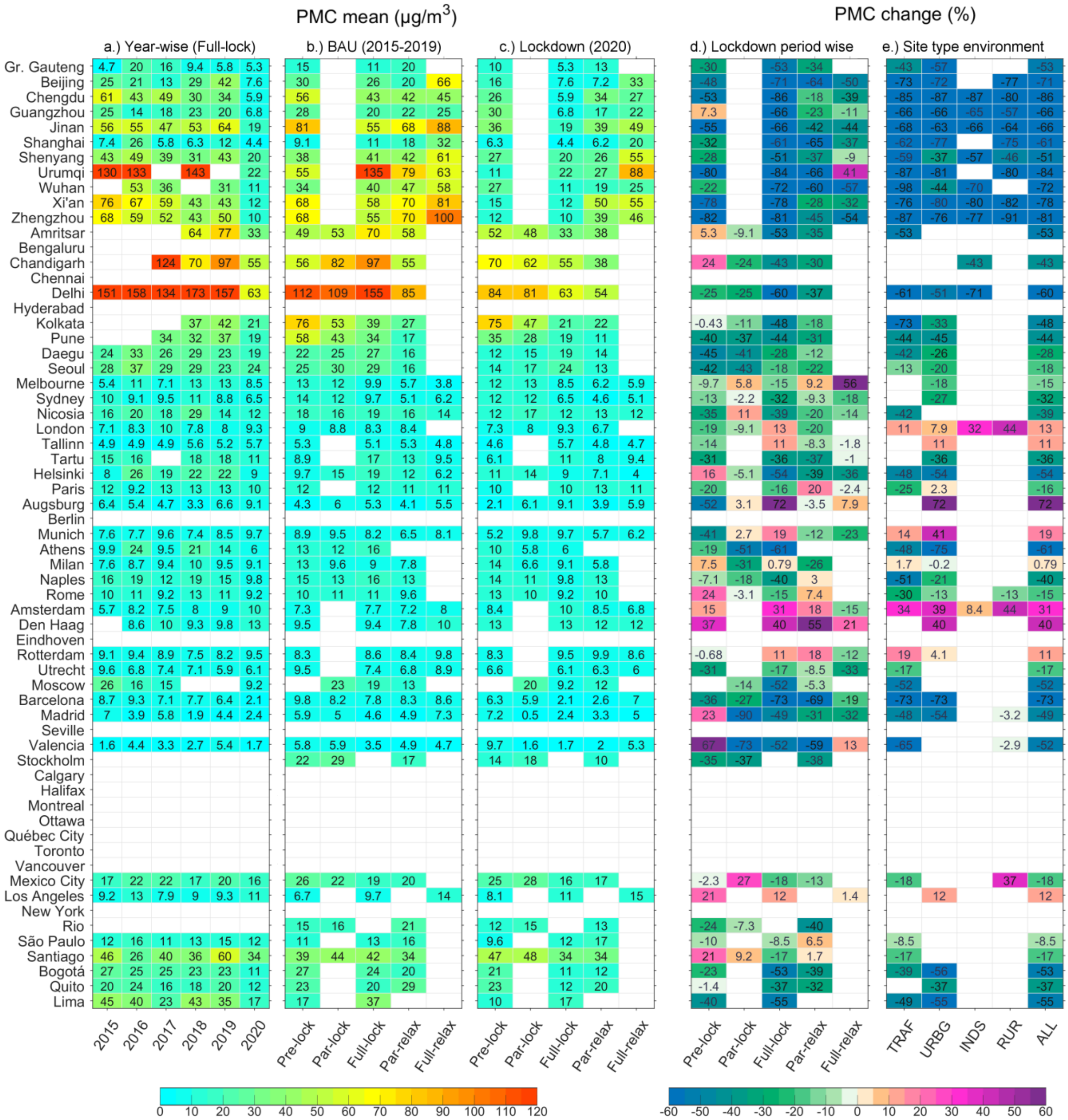

Figure S3.4.7. Observed concentrations (µg/m^3) and percentage changes in PMC (a) Mean concentrations for the equivalent full lockdown period for each year from 2015 to 2020, (b) Mean concentrations for different equivalent lockdown periods during BAU (2015-2019), (c) Observed mean concentrations during 2020 for different lockdown periods, (d) Percentage changes observed for different lockdown periods, and (e) Percentage changes observed for full lockdown in different environments.

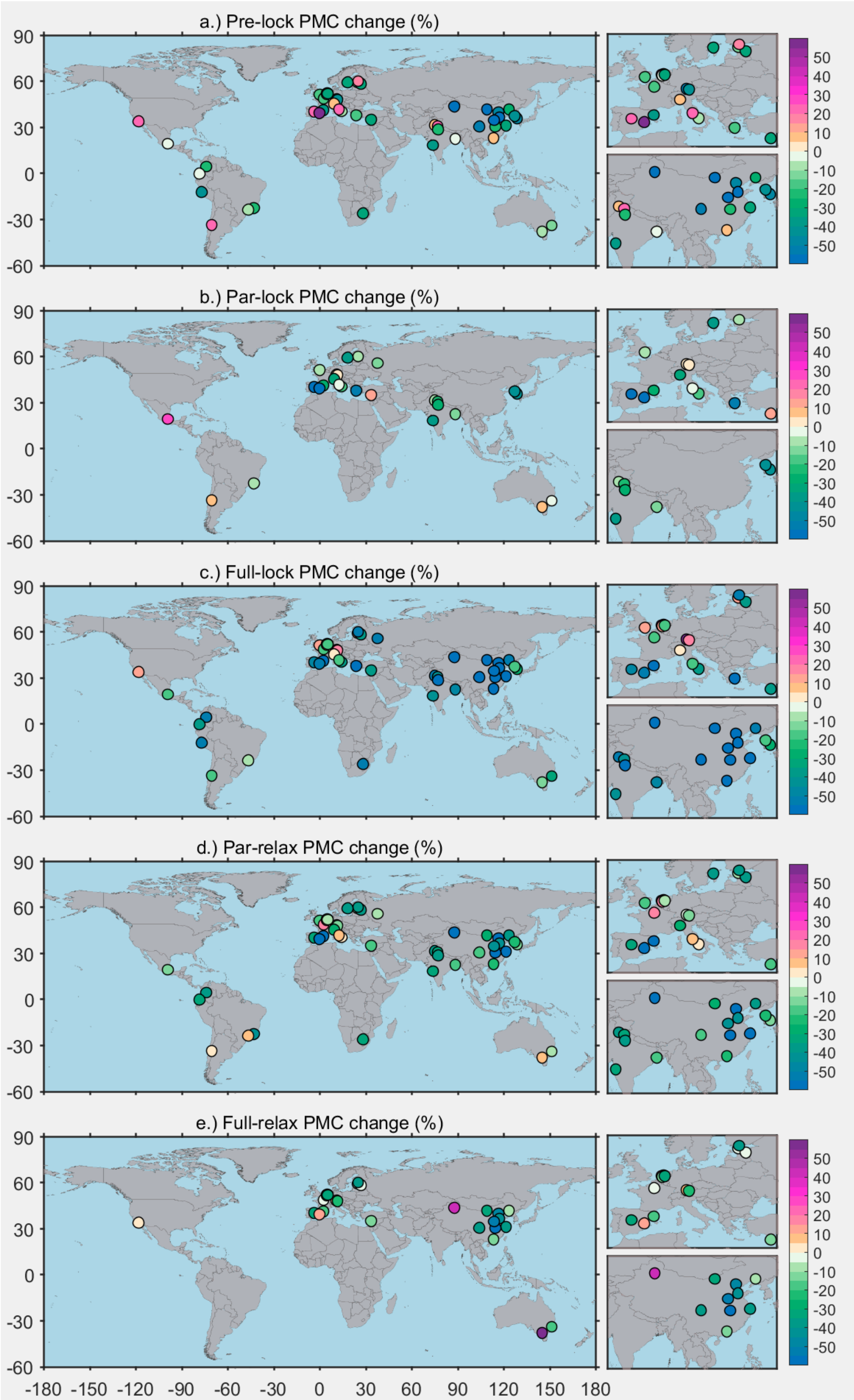

Figure S3.4.8. Observed percentage changes in PMC on global map for (a) pre-lockdown, (b) partial lockdown, (c) full lockdown, (d) partial relaxation, and (e) full relaxation. The small sub-panel maps show zoom of European and Asian countries.

Figure S3.4.9. Observed concentrations (µg/m³) and percentage changes in NO_2 (a) Mean concentrations for the equivalent full lockdown period for each year from 2015 to 2020, (b) Mean concentrations for different equivalent lockdown periods during BAU (2015-2019), (c) Observed mean concentrations during 2020 for different lockdown periods, (d) Percentage changes observed for different lockdown periods, and (e) Percentage changes observed for full lockdown in different environments.

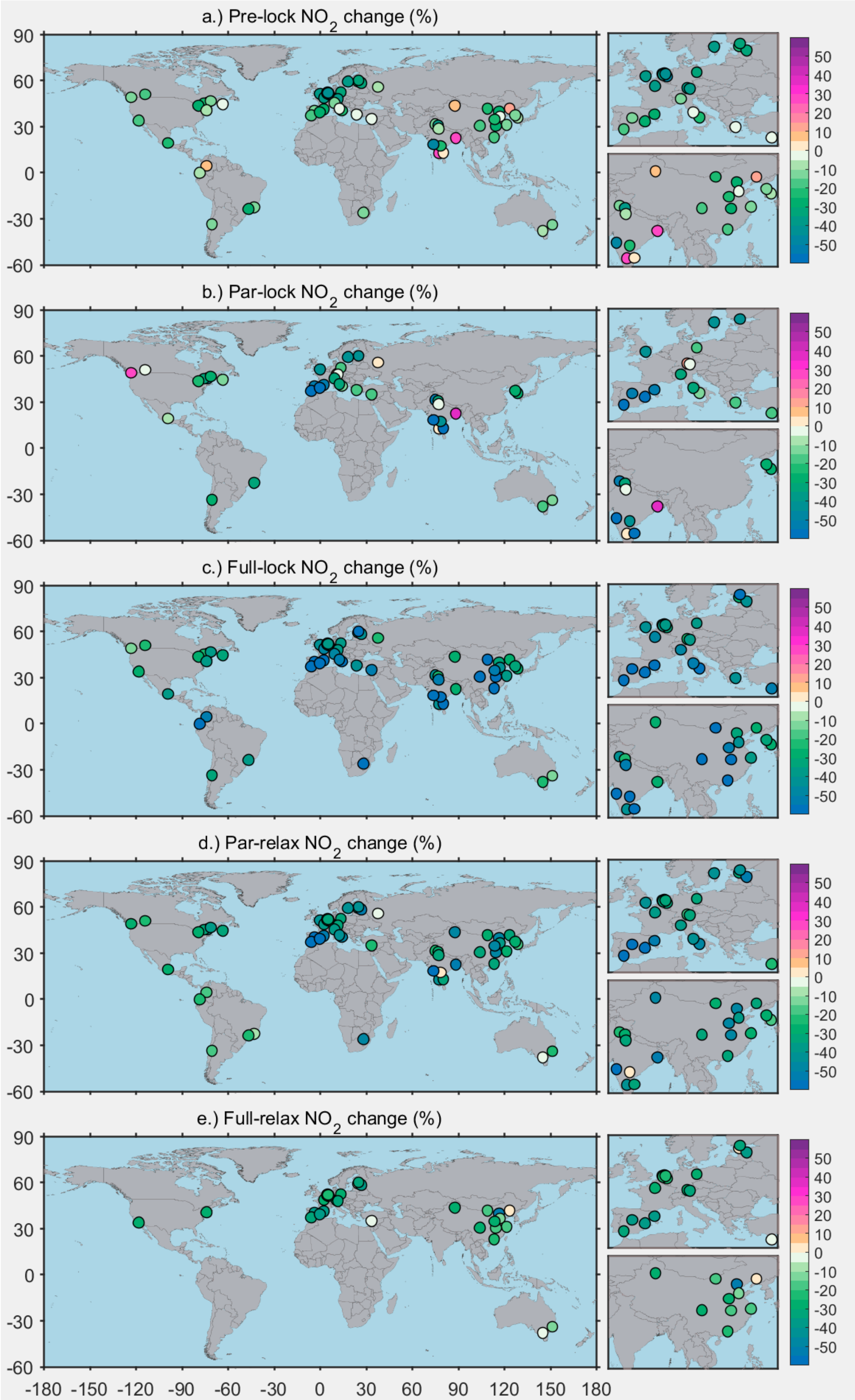

Figure S3.4.10. Observed percentage changes in NO_2 on global map for (a) pre-lockdown, (b) partial lockdown, (c) full lockdown, (d) partial relaxation, and (e) full relaxation. The small sub-panel maps show zoom of European and Asian countries.

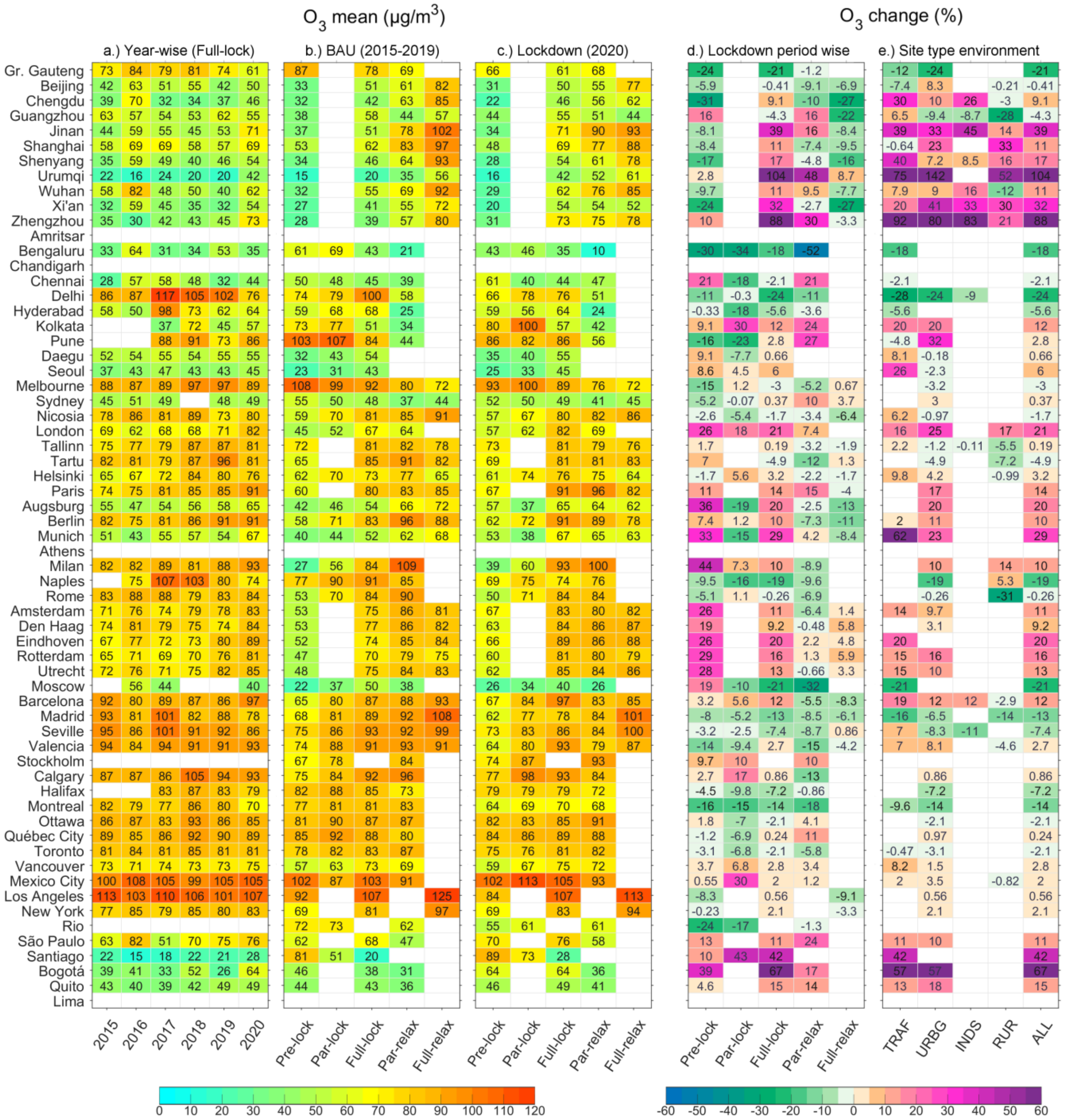

Figure S3.4.11. Observed concentrations (μg/m^3) and percentage changes in O_3 (a) Mean concentrations for the equivalent full lockdown period for each year from 2015 to 2020, (b) Mean concentrations for different equivalent lockdown periods during BAU (2015-2019), (c) Observed mean concentrations during 2020 for different lockdown periods, (d) Percentage changes observed for different lockdown periods, and (e) Percentage changes observed for full lockdown in different environments.

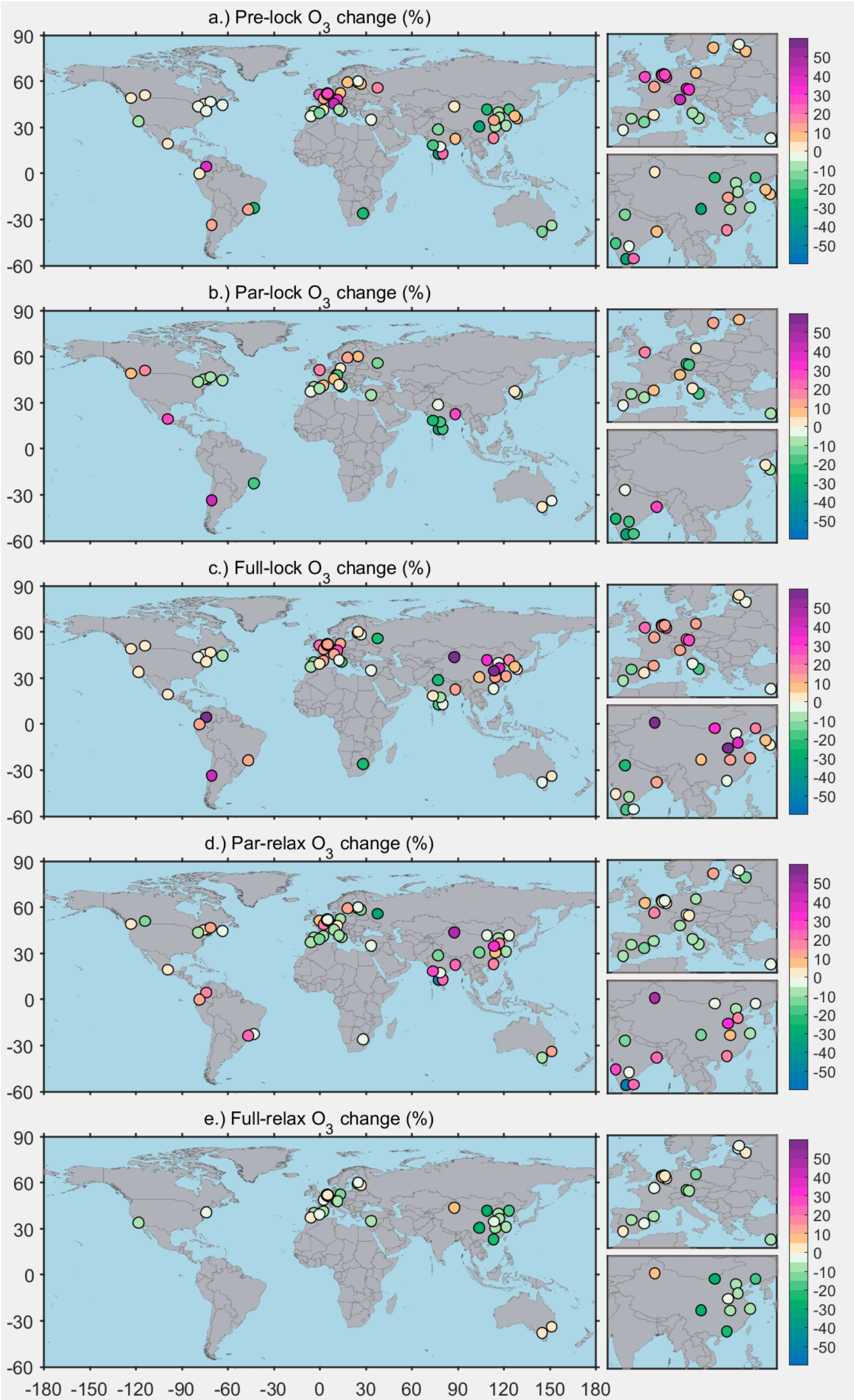

Figure S3.4.12. Observed percentage change in O_3 on global map for (a) pre-lockdown, (b) partial lockdown, (c) full lockdown, (d) partial relaxation, and (e) full relaxation. The small sub-panel maps show zoom of Europe and Asian countries.

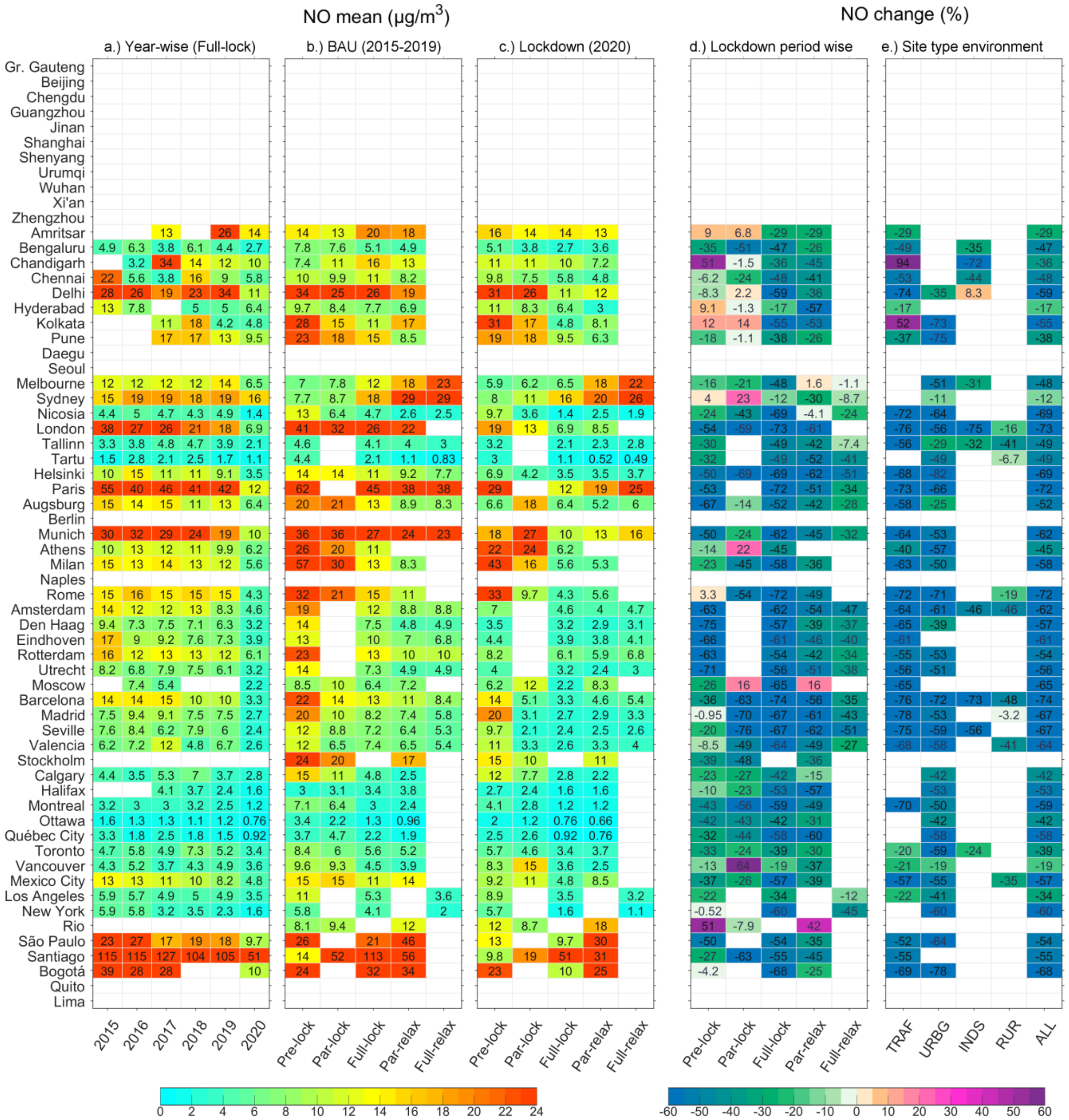

Figure S3.4.13. Observed concentrations (μg/m^3) and percentage changes in NO (a) Mean concentrations for the equivalent full lockdown period for each year from 2015 to 2020, (b) Mean concentrations for different equivalent lockdown periods during BAU (2015-2019), (c) Observed mean concentrations during 2020 for different lockdown periods, (d) Percentage changes observed for different lockdown periods, and (e) Percentage changes observed for full lockdown in different environments.

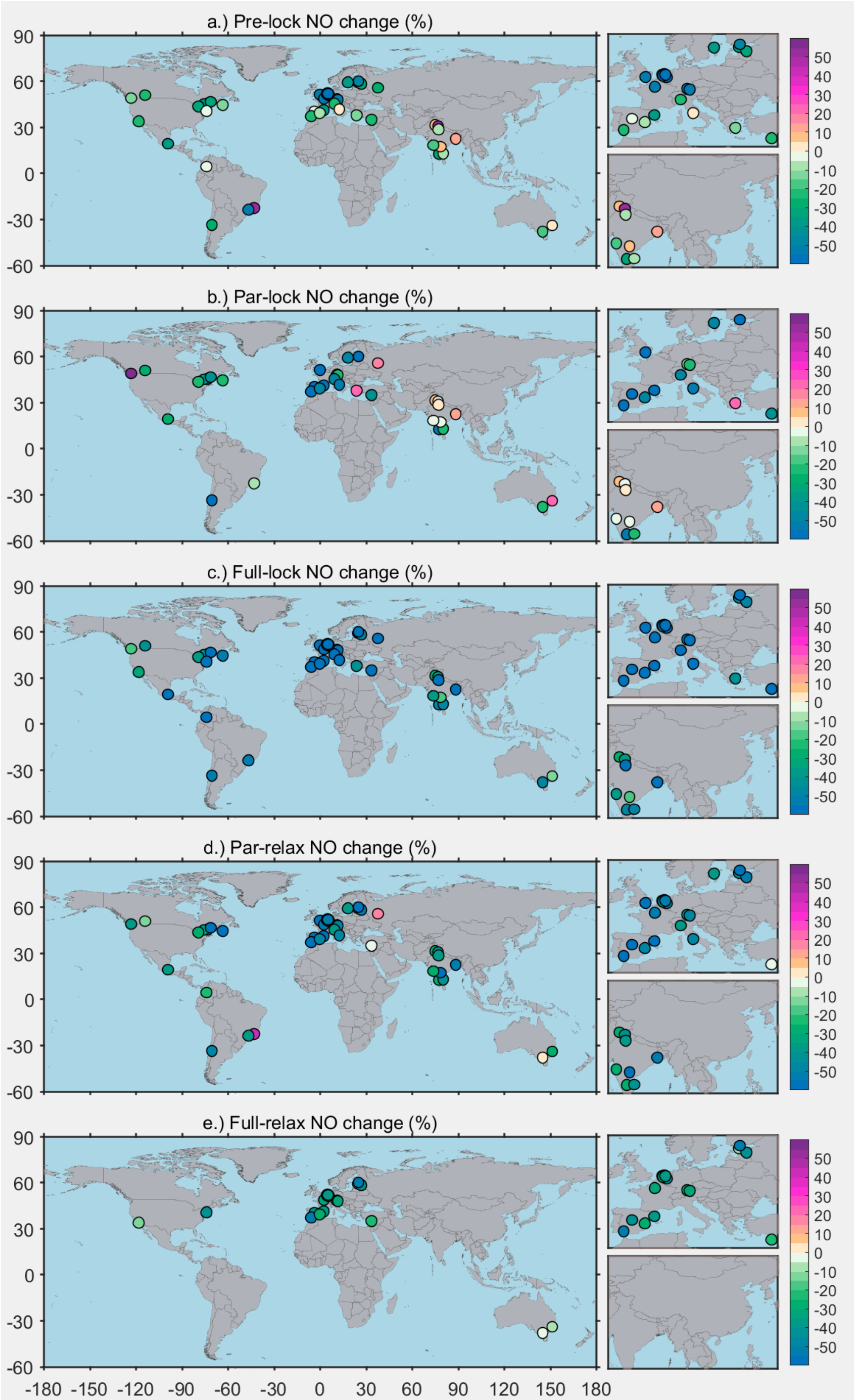

Figure S3.4.14. Observed percentage changes in NO on global maps for (a) pre-lockdown, (b) partial lockdown, (c) full lockdown, (d) partial relaxation, and (e) full relaxation. The small sub-panel maps show zoom of European and Asian countries.

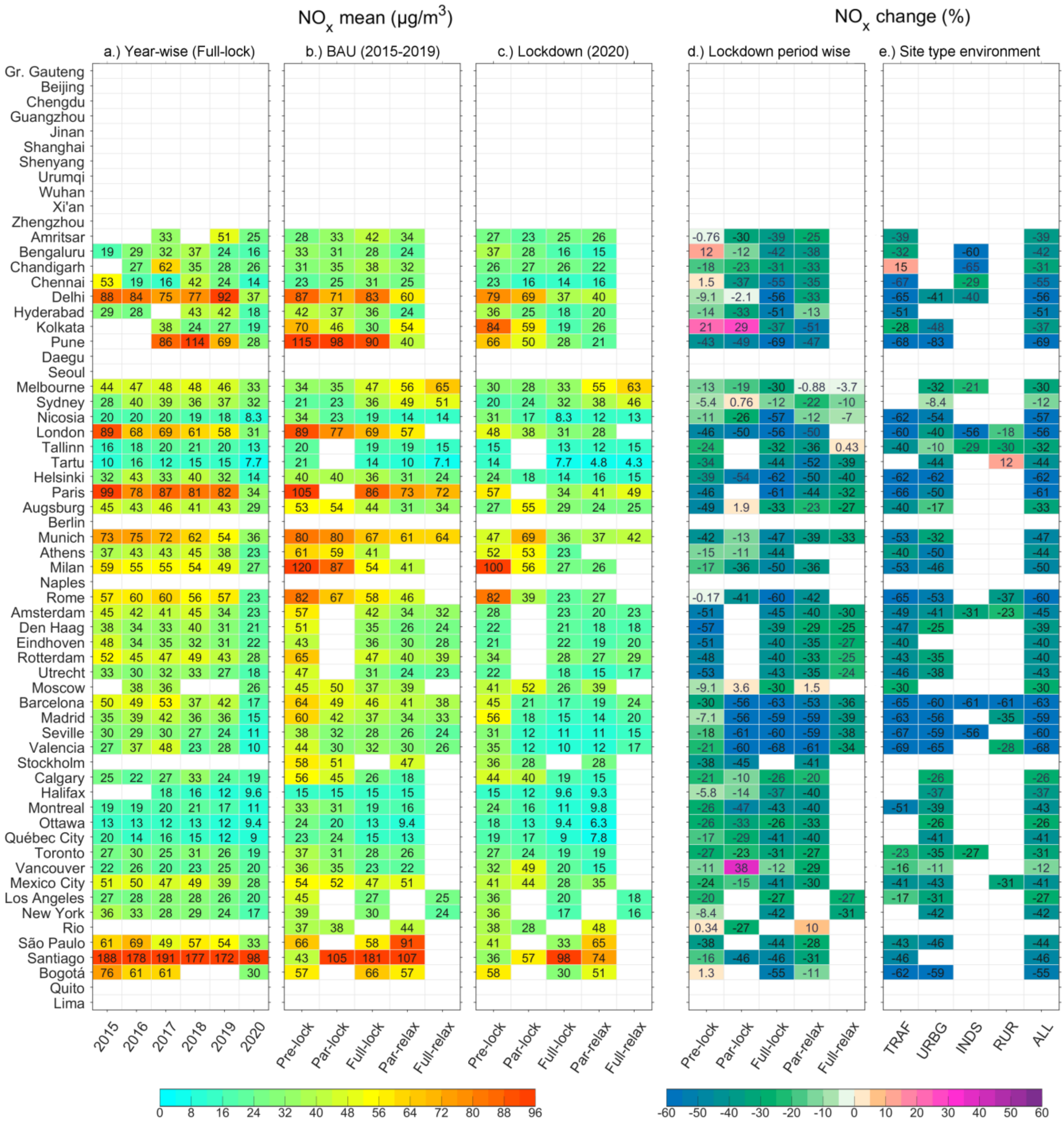

Figure S3.4.15. Observed concentrations (µg/m^3) and percentage changes in NO_X (a) Mean concentrations for the equivalent full lockdown period for each year from 2015 to 2020, (b) Mean concentrations for different equivalent lockdown periods during BAU (2015-2019), (c) Observed mean concentrations during 2020 for different lockdown periods, (d) Percentage changes observed for different lockdown periods, and (e) Percentage changes observed for full lockdown in different environments.

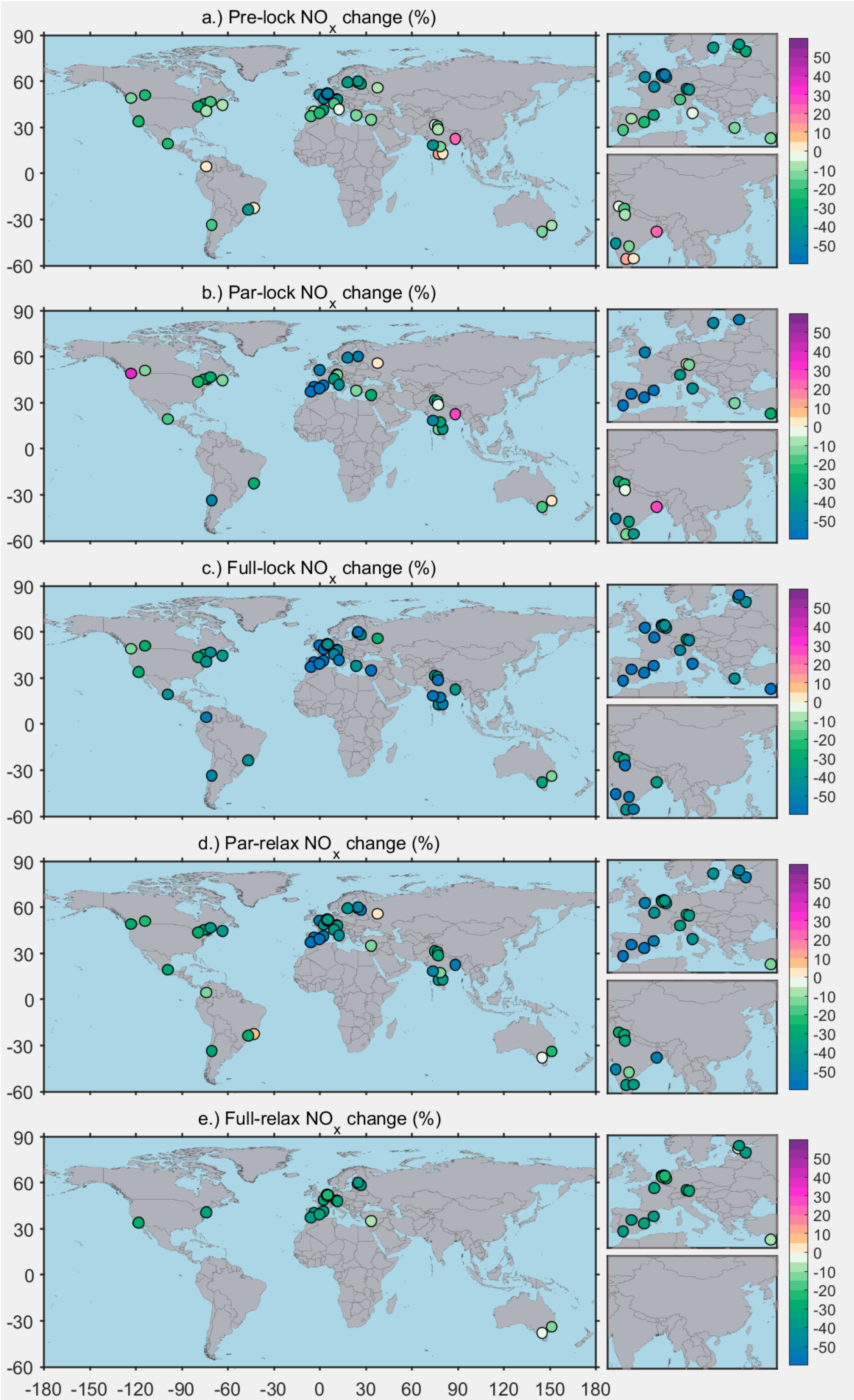

Figure S3.4.16. Observed percentage changes in NO_X on global maps for (a) pre-lockdown, (b) partial lockdown, (c) full lockdown, (d) partial relaxation, and (e) full relaxation. The small sub-panel maps show zoom of European and Asian countries.

Figure S3.4.17. Observed concentrations (μg/m^3) and percentage changes in CO (a) Mean concentrations for the equivalent full lockdown period for each year from 2015 to 2020, (b) Mean concentrations for different equivalent lockdown periods during BAU (2015-2019), (c) Observed mean concentrations during 2020 for different lockdown periods, (d) Percentage changes observed for different lockdown periods, and (e) Percentage changes observed for full lockdown in different environments.

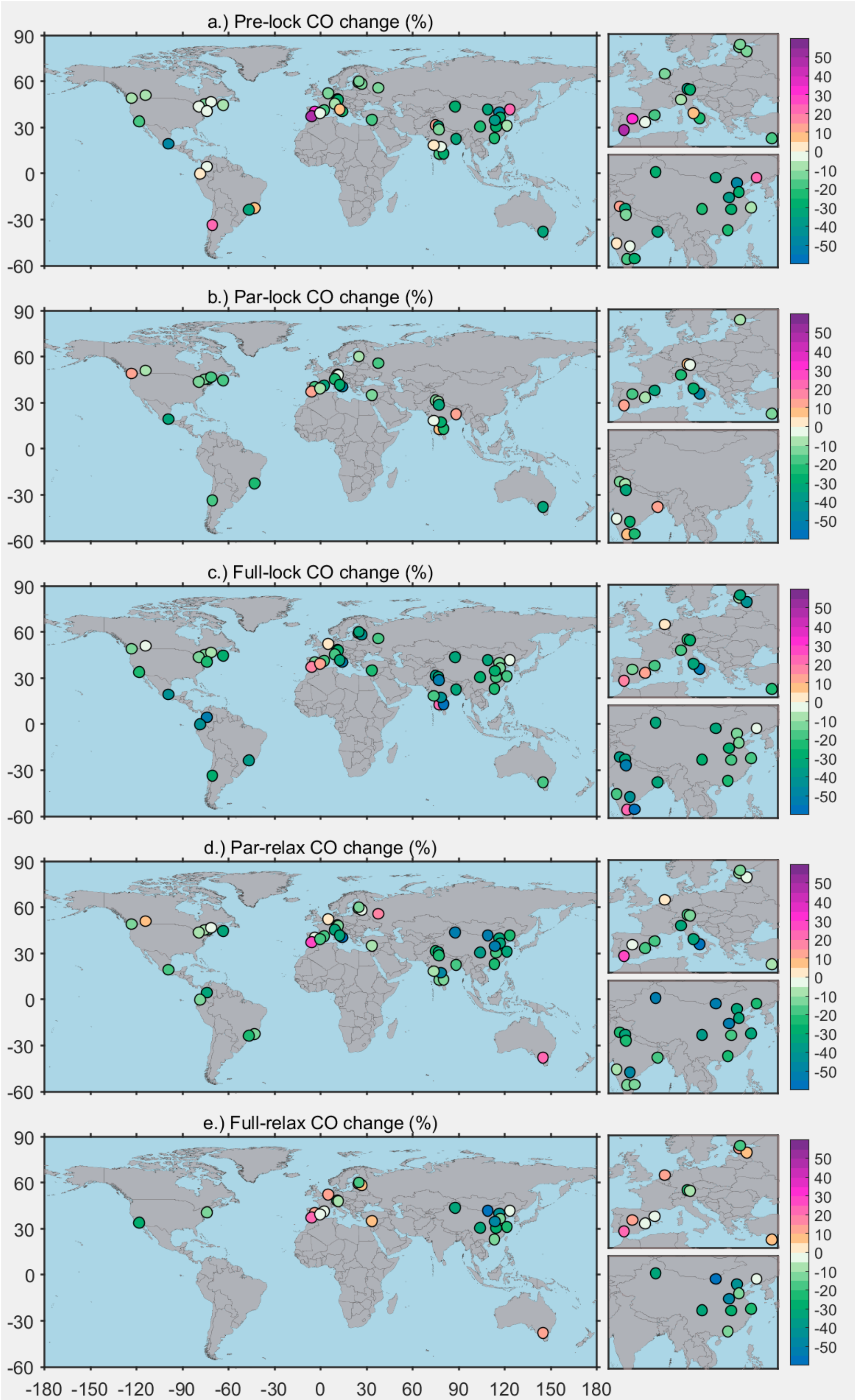

Figure S3.4.18. Observed percentage changes in CO on global map for (a) pre-lockdown, (b) partial lockdown, (c) full lockdown, (d) partial relaxation, and (e) full relaxation. The small sub-panel maps show zoom of European and Asian countries.

Figure S3.4.19. Observed concentration ratios and percentage changes in NO_2/CO concentration ratio (a) Mean concentration ratios for the equivalent full lockdown period for each year from 2015 to 2020, (b) Mean concentration ratios for different equivalent lockdown periods during BAU (2015-2019), (c) Observed mean concentration ratios during 2020 for different lockdown periods, (d) Percentage changes observed for different lockdown periods, and (e) Percentage changes observed for full lockdown in different environments.

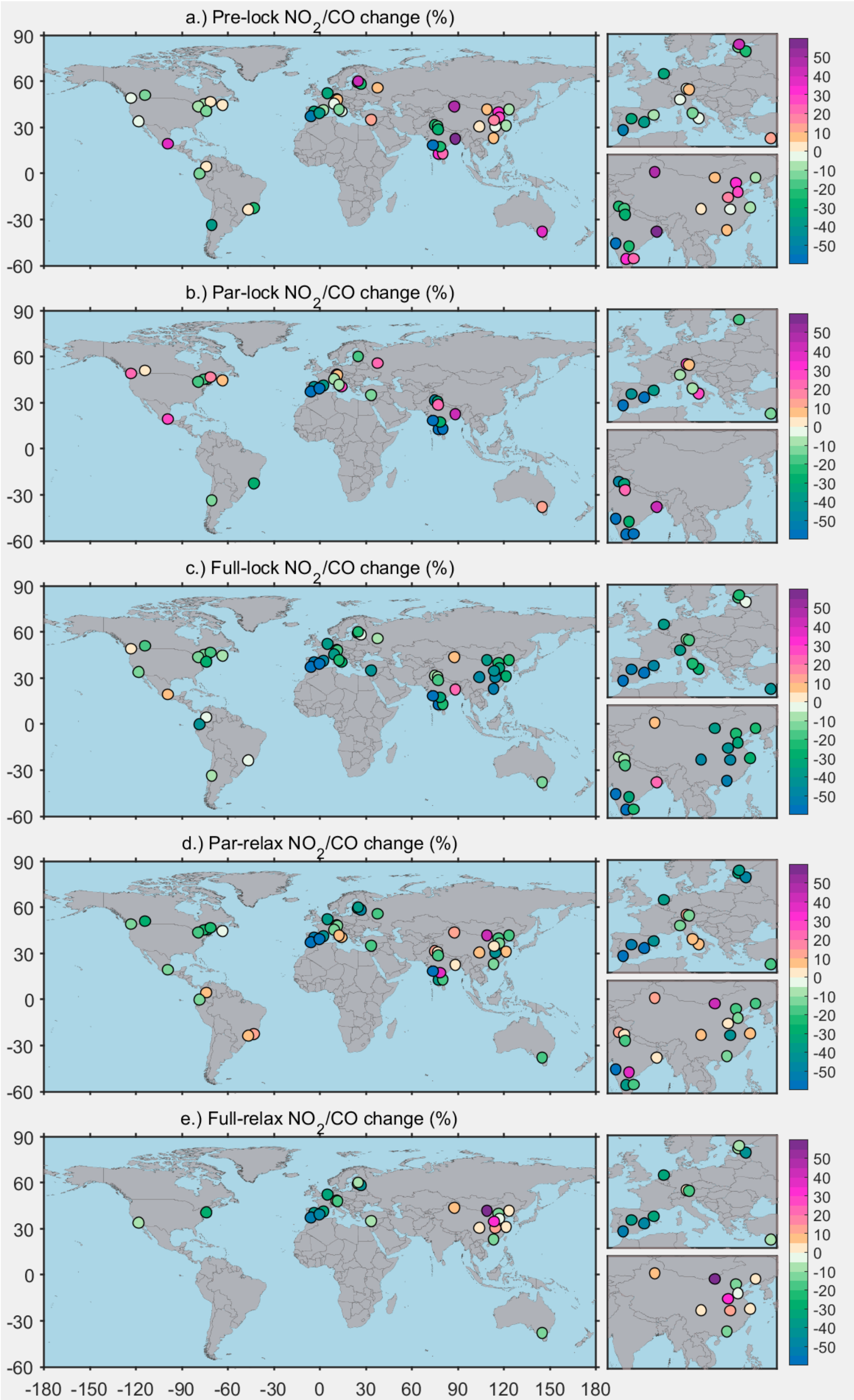

Figure S3.4.20. Observed percentage changes in NO_2/CO ratios on global maps for (a) pre-lockdown, (b) partial lockdown, (c) full lockdown, (d) partial relaxation, and (e) full relaxation. The small sub-panel maps show zoom of European and Asian countries.

Figure S3.4.21. Observed concentration ratios and percentage changes in NO_X/CO concentration ratio (a) Mean concentration ratios for the equivalent full lockdown period for each year from 2015 to 2020, (b) Mean concentration ratios for different equivalent lockdown periods during BAU (2015-2019), (c) Observed mean concentration ratios during 2020 for different lockdown periods, (d) Percentage changes observed for different lockdown periods, and (e) Percentage changes observed for full lockdown in different environments.

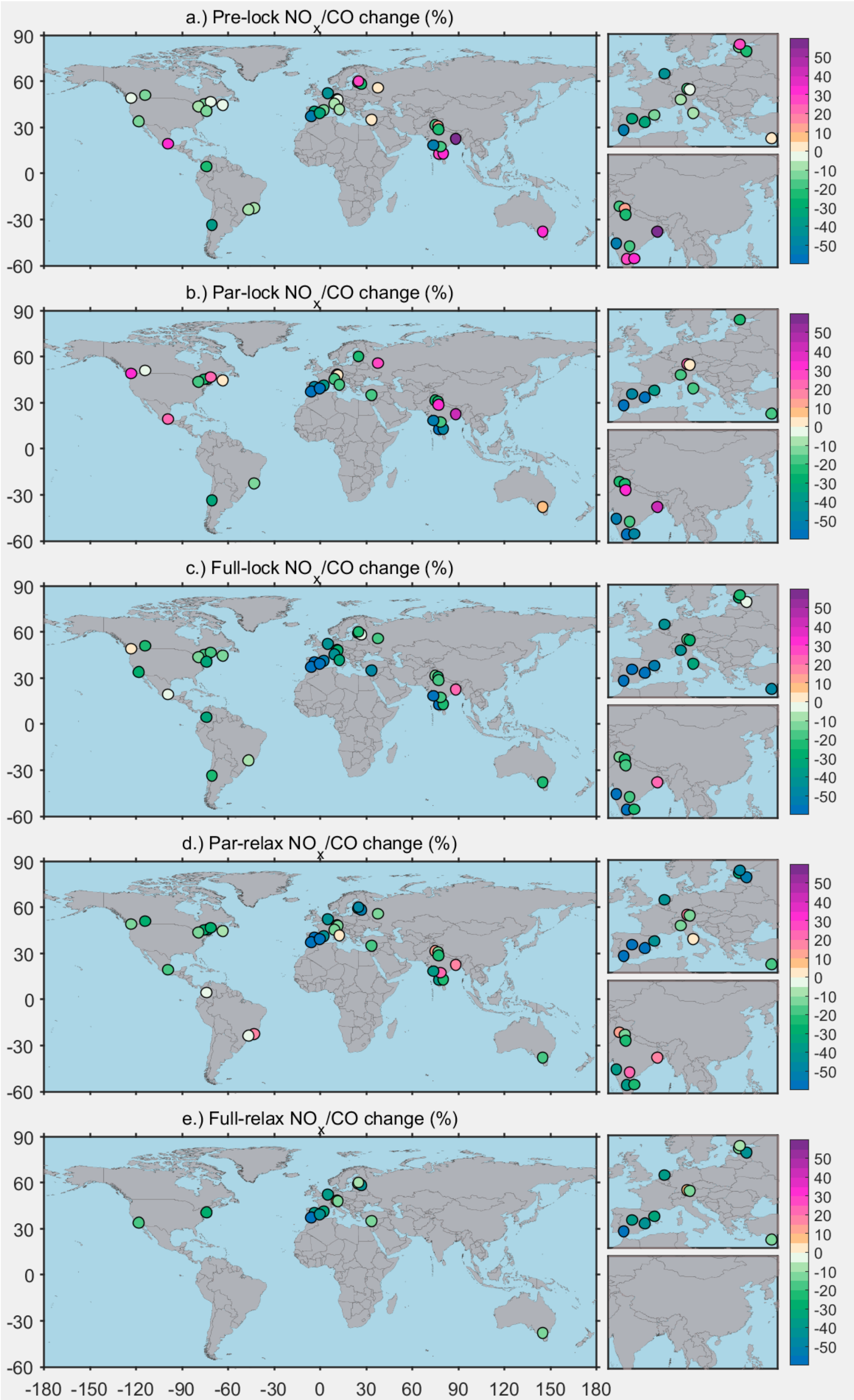

Figure S3.4.22. Observed percentage changes in NO_X/CO ratios on global maps for (a) pre-lockdown, (b) partial lockdown, (c) full lockdown, (d) partial relaxation, and (e) full relaxation. The small sub-panel maps show zoom of European and Asian countries.

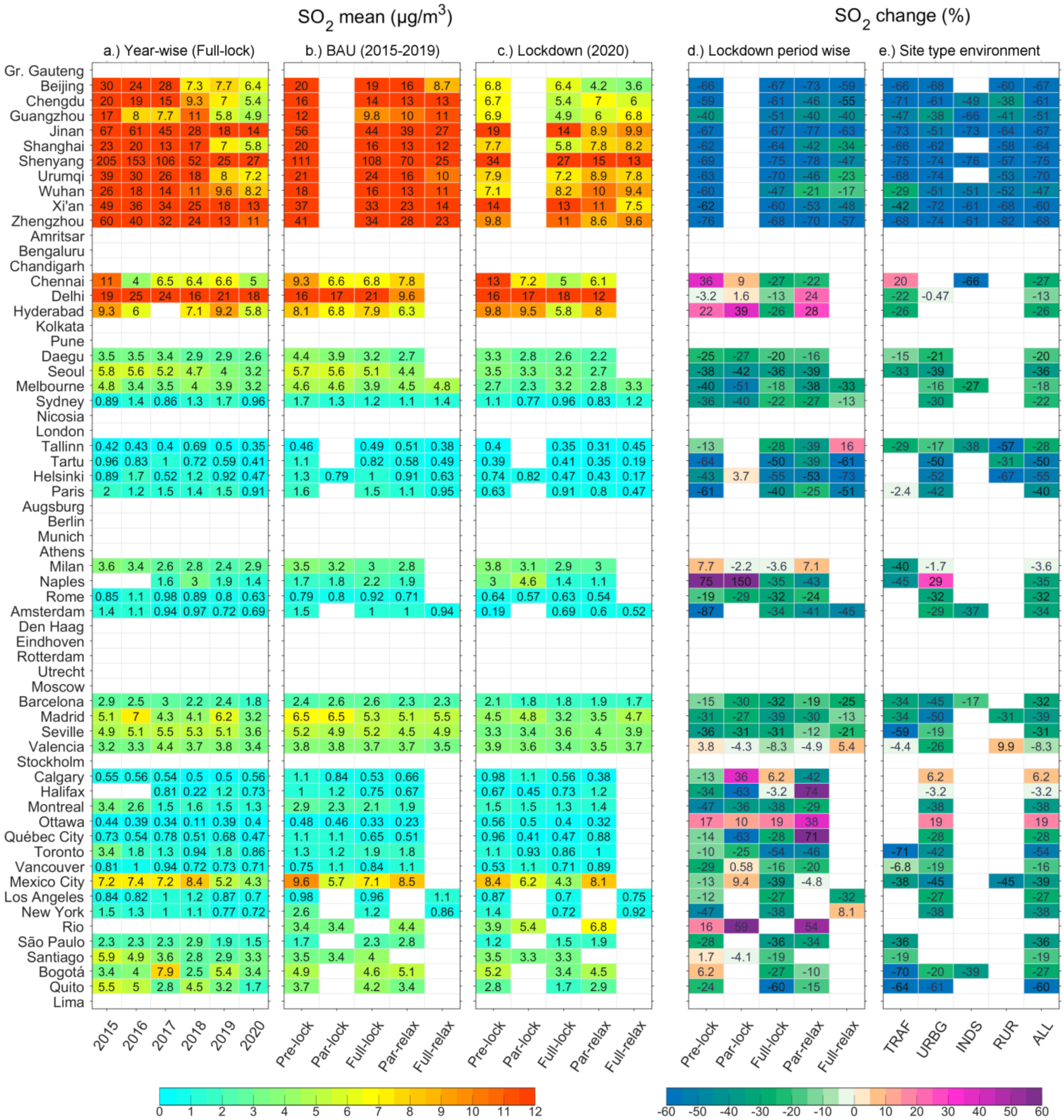

Figure S3.4.23. Observed concentrations (μg/m³) and percentage changes in SO_2 (a) Mean concentrations for the equivalent full lockdown period for each year from 2015 to 2020, (b) Mean concentrations for different equivalent lockdown periods during BAU (2015-2019), (c) Observed mean concentrations during 2020 for different lockdown periods, (d) Percentage changes observed for different lockdown periods, and (e) Percentage changes observed for full lockdown in different environments.

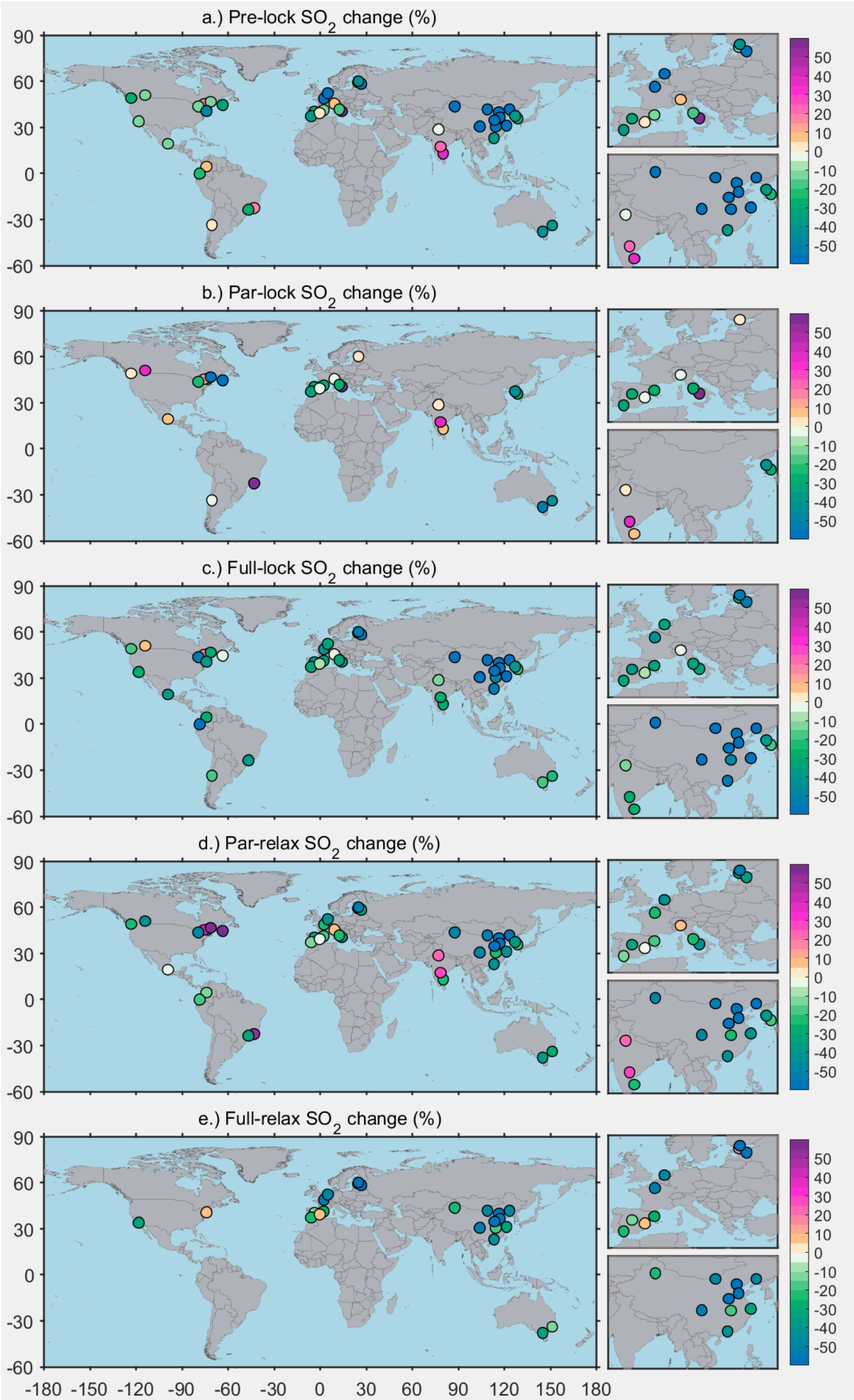

Figure S3.4.24. Observed percentage changes in SO_2 on global map for (a) pre-lockdown, (b) partial lockdown, (c) full lockdown, (d) partial relaxation, and (e) full relaxation. The small sub-panel maps show zoom of European and Asian countries.

Figure S3.4.25. Observed concentration ratios and percentage changes in NO_2/NO_X concentration ratio (a) Mean concentration ratios for the equivalent full lockdown period for each year from 2015 to 2020, (b) Mean concentration ratios for different equivalent lockdown periods during BAU (2015-2019), (c) Observed mean concentration ratios during 2020 for different lockdown periods, (d) Percentage changes observed for different lockdown periods, and (e) Percentage changes observed for full lockdown in different environments.

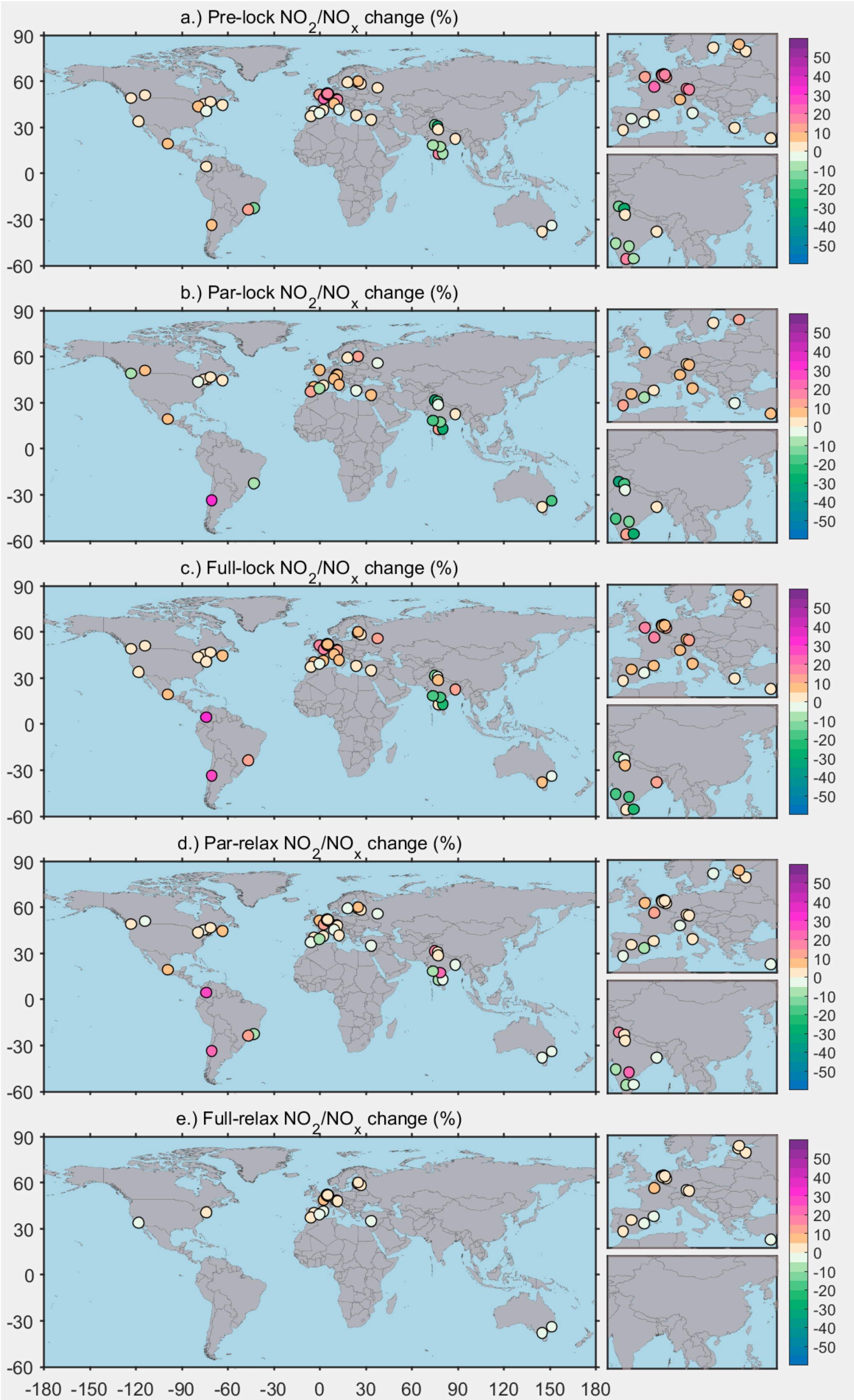

Figure S3.4.26. Observed percentage changes in NO_2/NO_X ratios on global maps for (a) pre-lockdown, (b) partial lockdown, (c) full lockdown, (d) partial relaxation, and (e) full relaxation. The small sub-panel maps show zoom of European and Asian countries.

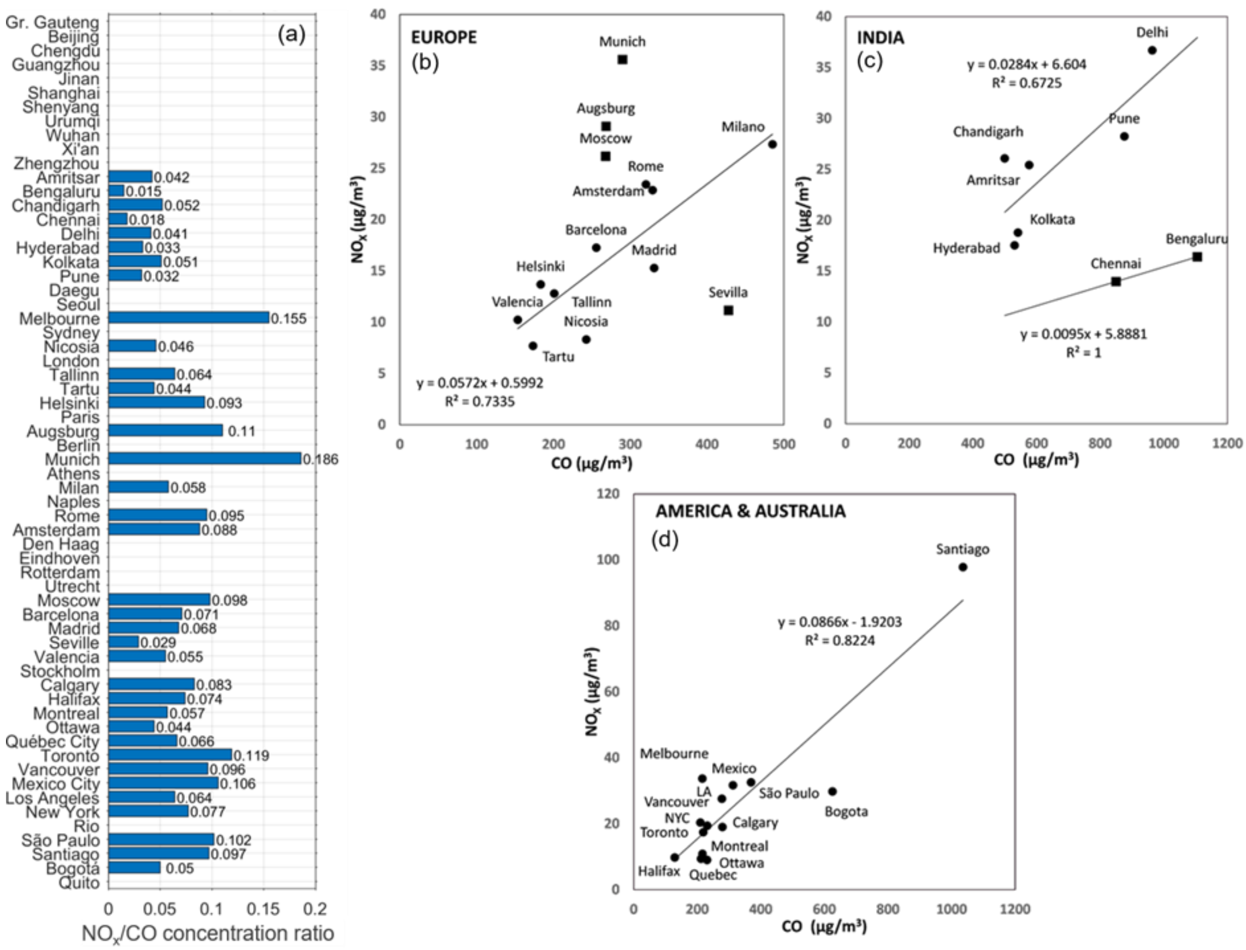

Figure S3.4.27. Ratio of NO_X/CO as a mean over the 2020 full lockdown period shown as (a) bar plot for each city, and (b-d) cross correlation plots for the cities grouped by regions.

Table S3.4.1. Mean concentration deltas and percentage changes inf NO_2, O_3, NOx and Ox in 2020 compared to the same period in 2015-2019. Also shown are the slopes and intercepts, their 95% confidence intervals (C.I.) and the fraction of NO_2 within OX.

Country and period of data analysis	City (site)	Site type	**<u>Mean</u>** daytime (8:00 – 17:00) changes ppb and [%]: δ8hO_3	δO_3	δNOx	δNO_2	δOX	**2015-2019** Slope [95% C.I.]	**2015-2019** Intercept [95% C.I.] ppb	**2015-2019** NO_2/OX	**2020** Slope [95% C.I.]	**2020** Intercept [95% C.I.] ppb	**2020** NO_2/OX
Spain March 16 – July 31	Barcelona (Eixample)	Urban	3.3 [9.9%]	2.3 [8.4%]	-36.2 [-58.3%]	-15.9 [-51.7%]	-13.6 [-23.5%]	0.19 [0.17; 0.21]	46 [44; 47]	0.53	0.23 [0.16; 0.30]	38 [36; 40]	0.33
	Barcelona (Tona)	Rural	-8.3 [-15.2%]	-7.2 [-15.8%]	-3.9 [-50.4%]	-3.2 [-54.6%]	-10.3 [-19.9%]	0.10 [-0.1; 0.3]	51 [49; 53]	0.11	1.0 [0.14; 1.9]	38 [34; 41]	0.06
	Madrid (Aguirre)	Urban	2.2 [5.3%]	2.4 [7.1%]	-24.0 [-59.9%]	-13.1 [-50.6%]	-10.7 [-18.0%]	0.14 [0.10; 0.17]	54 [52;56]	0.43	0.54 [0.37;0.71]	40 [37; 43]	0.26
	Madrid (El Atazar)	Rural	-7.5 [-13.5%]	-5.9 [-12.3%]	-0.6 [-21.0%]	-0.5 [-28.2%]	-6.4 [-12.8%]	0.44 [-0.16; 1.0]	49 [47;51]	0.04	11 [8.3; 13]	21 [15;26]	0.03
Italy	Milan (Pascal)	Urban background	-0.9 [-1.8%]	-1.0 [-2.7%]	-10.7 [-44.3%]	-6.2 [-41.9%]	-7.0 [-13.1%]	-0.12 [-0.17; -0.07]	56 [55;58]	0.30	-0.14 [-0.28; 0.01]	48 [46;51]	0.20
	Milan (Saronno)	Urban	-0.1 [-0.3%]	0.7 [1.7%]	-6.6 [-41.9%]	-5.0 [-44.6%]	-4.3 [-7.8%]	-0.33 [-0.41;	60 [59;62]	0.23	-0.41 [-0.62;	55 [52;57]	0.14

February 25 – July 31								-0.25]			-0.19]		
	Rome (Cipro)	Urban background	1.6 [4.3%]	1.7 [5.2%]	-13 [-47.4%]	-7.7 [-42.7%]	-6.0 [-11.9%]	0.09 [0.05; 0.13]	48 [47;49]	0.36	0.19 [0.04; 0.35]	41 [39;44]	0.23
	Rome (Guido)	Rural	-12.3 [-25.3%]	-10.7 [-24.4%]	-1.3 [-29.9%]	-0.9 [-26.4%]	-11.2 [-23.9%]	-0.02 [-0.22; 0.18]	47 [46;48]	0.07	0.46 [-0.02; 0.94]	34 [32;36]	0.07
England	London (Marylebone)	Urban	11.4 [63.6%]	11.1 [88.1%]	-87.7 [-71.4%]	-31.9 [-61.5%]	-20.8 [-32.2%]	0.19 [0.18; 0.20]	41 [39;42]	0.78	0.16 [0.10; 0.23]	38 [35;41]	0.45
March 5 – July 31	Chilbolton	Rural	1.6 [3.8%]	1.6 [4.5%]	-2.0 [-37.0%]	-1.8 [-38.8%]	-0.2 [-0.5%]	0.59 [0.36; 0.82]	38 [36;39]	0.12	2.8 [2.0; 3.5]	38 [28;39]	0.07
Brazil	São Paulo (Pinheiros)	Urban	4.6 [21.9%]	4.2 [24.6%]	-19.1 [-42.8%]	-8.0 [-38.9%]	-3.9 [-10.4%]	0.12 [0.08; 0.16]	32 [30;35]	0.57	0.08 [0.01; 0.16]	32 [29;34]	0.38
March 23 – July 19	São Paulo (Pico Jaraguá) **(No data for 2015-2016)**	Mountain site	-0.5 [-1.5%]	-1.5 [-5.0%]	-4.1 [-36.4%]	-2.4 [-29.2%]	-4.0 [-10.6%]	0.02 [0.01; 0.4]	36 [33;37]	0.23	0.12 [-0.32; 0.54]	32 [29;36]	0.17
	Delhi	Urban	-11.8	-11.2	-12.2	-10.6	-22.4	0.98	30	0.41	-0.39	35	0.39

India March 16-September 30	(Puram) **(data available until August 31, 2020)**		[-35.7%]	[-34.7%]	[-52.2%]	[-52.5%]	[-41.8%]	[0.76; 1.1]	[28;36]		[-0.88; 0.1]	[30; 41]	
	Delhi (Shadipur)	Urban	-1.9 [-7.0%]	-1.9 [-7.9%]	-6.3 [-31.6%]	-5.9 [-37.4%]	-8.2 [-20.0%]	0.76 [0.63; 0.89]	25 [22;28]	0.39	-1.1 [-1.6; -0.5]	47 [39; 55]	0.42
Canada March 15 – May 31	Toronto (Toronto West)	Urban	-1.2 [-3.1%]	1.6 [4.9%]	-6.7 [-40.3%]	-4.4 [-39.5%]	-2.8 [-6.3%]	0.08 [-0.01; 0.18]	42 [41;44]	0.26	-0.38 [-0.69; -0.07]	45 [41; 48]	0.17
Chile March 26 – July 31	Santiago (Puente Alto)	Urban	4.8 [22.5%]	3.5 [18.6%]	-31.0 [-40.3%]	-10.1 [-39.7%]	-6.2 [-14.3%]	0.16 [0.13; 0.18]	33 [32;36]	0.58	0.06 [-0.04; 0.15]	36 [32; 39]	0.43
Colombia March 20 – June 30	Bogotá (Carvajal)	Urban	5.2 [39.4%]	5.0 [39.4%]	-18.2 [-26.0%]	-6.7 [-27.2%]	-2.1 [-5.9%]	-0.01 [-0.05; 0.05]	36 [32;40]	0.69	-0.02 [-0.11; 0.03]	34 [32;40]	0.54
China January 1 – May 9	Wuhan (Qingshan Ganghua)	Urban	6.0 [41.9%]	6.3 [21.3%]	-15.3 [-47.8%]	-9.0 [-39.4%]	-2.7 [-5.2%]	0.09 [0.03; 0.15]	50 [47;52]	0.46	0.03 [-0.26; 0.32]	49 [43; 54]	0.31

South Africa March 27 – May 31	Greater Gauteng (Kliprivier)	Urban	0.8 [2.4%]	-0.65 [-2.3%]	-13.5 [-33.6%]	-2.6 [-17.5%]	-2.5 [-5.6%]	0.12 [0.07; 0.14]	37 [36;40]	0.35	0.29 [0.23; 0.37]	32 [30; 34]	0.29
Australia March 16 – June 30	Sydney (Rozelle)	Urban	4.6 [26.3%]	2.8 [18.3%]	-4.7 [-22.0%]	-2.2 [-19.7%]	0.6 [2.4%]	-0.01 [-0.03; 0.04]	26 [25;27]	0.43	-0.04 [-0.06; 0.18]	26 [24;28]	0.30
	Sydney (Bargo)	Urban backgrou nd	-2.2 [-8.1%]	-1.3 [-5.6%]	-0.5 [-10.3%]	-0.5 [-16.5%]	-1.8 [-6.7%]	-0.02 [-0.08; 0.05]	26 [25;27]	0.11	-0.12 [-0.27; -0.01]	25 [24;26]	0.10

S4.1 Regional changes in air quality during full lockdown

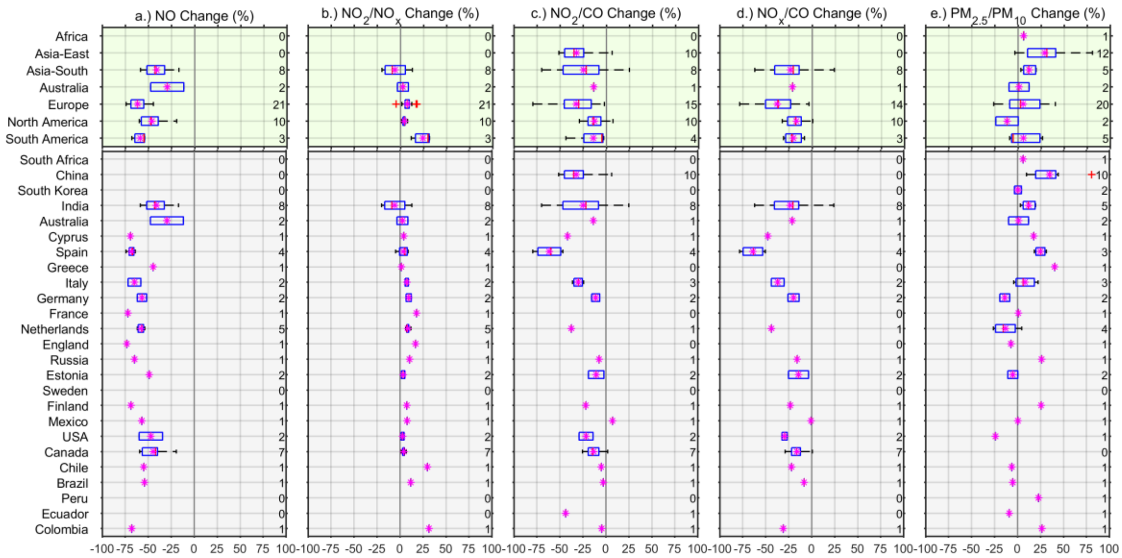

Figure S4.1.1. Continental/country-wide changes in air pollution shown as boxplots for the full lockdown period for (a) NO, (b) NO_2/NO_X, (c) NO_2/CO, (d) NO_X/CO, (e) $PM_{2.5}/PM_{10}$. Numbers on the right-hand side of the panels indicate number of cities. The red + symbol is the outlier (values more than 1.5 times the interquartile range)